Fuel 405 (2026) 136479

Contents lists available at ScienceDirect

Fuel

journal homepage: www.elsevier.com/locate/fuel

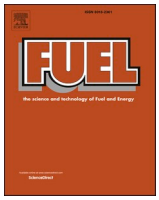

Full Length Article

A CFD-driven machine learning approach for predicting PEM electrolyzer performance

Safiye Nur Ozdemir [a,*], Oguzhan Pektezel [b]

[a] Department of Mechanical Engineering, University of Sakarya, 54050 Adapazari, Turkey
[b] Department of Mechanical Engineering, University of Balikesir 10145 Balikesir, Turkey

ARTICLE INFO

Keywords:
PEM electrolyzer
CFD simulation
Machine learning
Current density

ABSTRACT

Proton exchange membrane electrolyzers (PEMELs) powered by renewable energy sources represent a next-generation technology for producing green hydrogen. The performance of PEMEL can be greatly enhanced by optimizing design parameters and operating conditions. This study presents the development of a full-scale, three-dimensional, two-phase computational fluid dynamics (CFD) model aimed at investigating the electrochemical performance of PEMELs under various physical conditions. Numerical simulations were conducted to evaluate the impact of four key physical parameters—temperature, porous transport layer (PTL) thickness, membrane thickness, and cell voltage—on the performance of the PEMEL. Based on the CFD results, four different machine learning (ML) algorithms—Support Vector Machine (SVM), Multilayer Perceptron (MLP), M5P, and Elastic Net—were trained and tested to predict the current density of the PEMEL. The effectiveness of each ML model was assessed using Mean Absolute Error (MAE) and Root Mean Squared Error (RMSE) metrics for both the training and testing datasets. Among the models, the SVM demonstrated superior predictive accuracy, achieving an MAE of 0.0068, an RMSE of 0.0108 during training, an MAE of 0.0202, and an RMSE of 0.0371 during testing. Moreover, with the SVM method, the R^2 value was found to be 0.9996 for the training set and 0.9953 for the test set, while the a20-index was determined as 93.9 % for the training set and 90.5 % for the test set. ML based on CFD analysis results before fabricating PEM electrolyzers enables rapid performance predictions for new designs, significantly reducing computational time and costs.

1. Introduction

In recent years, the rapid growth of the global population, the depletion of fossil fuel resources, accelerated industrialization, rising air pollutant emissions, concerns about global warming, and a shift toward modern lifestyles have all significantly heightened interest in clean, renewable, and sustainable energy sources [1,2]. Solar and wind energy are notable renewable sources for their low greenhouse gas emissions and minimal environmental impact. However, significant challenges arise in energy storage and utilization due to the variable and intermittent nature of energy production. Fortunately, hydrogen energy technologies have great potential for clean energy transformation. They can be produced from renewable sources and stored with fuel cells or power-to-gas systems, and their utilization is increasingly widespread across various sectors. Hydrogen production from fossil fuels emits significant carbon dioxide, which raises concerns about environmental sustainability. Therefore, producing green hydrogen through renewable energy and water electrolysis is a vital and promising technology. The main device used for water electrolysis in hydrogen production is the electrolyzer, which can be adjusted based on the required output [3,4]. Proton exchange membrane (PEM) electrolyzers represent an excellent solution for integrating renewable energy sources. Their ability to operate effectively across a broad range of current densities, coupled with high-efficiency hydrogen production and a rapid response to fluctuations in power supply, makes them an ideal choice for such applications. Additionally, PEM electrolyzer plants can easily establish a supply–demand balance due to their rapid response capability, enhancing their appeal in industrial applications [5,6]. The primary challenge in producing high-purity hydrogen using PEM electrolyzer technology is the high cost of noble metal-based electrocatalysts, such as iridium oxide (IrO_2) and ruthenium oxide (RuO_2), particularly in the anode side. As a result, most research in the literature focused on developing alternative catalysts that can help reduce these costs [7–9]. Due to the high costs of experimental tests assessing the performance and efficiency of PEM electrolyzers, mathematical modeling plays a

* Corresponding author at: Department of Mechanical Engineering, University of Sakarya, TR-54050, Sakarya, Turkey.
E-mail address: safiyeozdemir@sakarya.edu.tr (S.N. Ozdemir).

https://doi.org/10.1016/j.fuel.2025.136479
Received 9 June 2025; Received in revised form 25 July 2025; Accepted 5 August 2025
Available online 9 August 2025

Nomenclature

CCC	Cathode current collector
CFD	Computational Fluid Dynamics
ACL	Anode catalyst layer
CCL	Cathode catalyst layer
ACC	Anode current collector
CFC	Cathode flow channel
AFC	Anode flow channel
GA	Genetic Algorithm
PEMEL	Proton Exchange Membrane Electrolyzer
PTL	Porous Transport Layer
APTL	Anode porous transport layer
CPTL	Cathode porous transport layer
ML	Machine Learning
SVM	Support Vector Machine
MLP	Multilayer Perceptron
MAE	Mean Absolute Error
MEA	Membrane electrode assembly
sd	Standard deviation
S	Data instances
RF	Random Forest
RMSE	Root Mean Squared Error
VOF	Volume of Fluid
ANN	Artificial Neural Networks
R^2	Regression coefficient
$\vec{u}$	Velocity field (m/s)
σ	Pearson half-width
w	Peak tailing factor
x_i, x_j	Vector arguments
ω^T	Transpose of the weight vector
b	Bias
x	Input feature vector
x_i	Actual value
y_i	Predicted value
n	Number of data points
β	Regression vector
α	Elasticity parameter
λ	Regularization parameter
l	Norm
$P_\alpha(\beta)$	Penalty
ρ	Fluid density (kg/m^3)
P	Pressure (Pa)
T	Temperature (K)
μ	Dynamic viscosity (N/m^{2}s)
$\vec{F}$	Body force vector (N/m^3)
c_p	Specific heat (J/kgK)
k	Thermal conductivity (W/mK)
σ_{eff}	Effective electrical conductivity (S/m)
D	Diffusion coefficient (m^2/s)
M	Molar mass (kg/mol)
R	Universal gas constant (J/molK)
F	Faraday constant (C/mol)

crucial role in analyzing the behavior of systems. Particularly, CFD simulations are a powerful tool for analyzing the influence of design and operating parameters on the performance of PEM electrolyzers. Numerous numerical and experimental studies in the literature focus on enhancing the performance of PEM electrolyzers.

Hu et al. [10] developed a 2D CFD model for an electrolysis cell. Their study examined how three different operating parameters affect the energy efficiency of the PEM electrolyzer system. These parameters include the anode input flow rate, the cathode input flow rate, and the applied operating voltage. Under the optimal operating conditions, an energy efficiency of 79 % was achieved. Wang et al. [11] compared the nickel foam flow field with a conventional flow field. They found that using metal foam enhances the uniformity of the water and current density distributions. The investigation into the impact of nickel foam porosity on electrochemical performance revealed that performance enhancements correlated with a reduction in porosity. Notably, the most favorable results were observed at a porosity of 0.55. Tirumalasetti et al. [12] analyzed the double-layered wire mesh (DLWM) flow channel in PEM electrolyzers. They discovered that this design outperforms conventional models, achieving up to a 61 % increase in hydrogen production. Additionally, the DLWM improves mass transport, further enhancing electrolysis efficiency. Saidi et al. [13] developed a mathematical model to analyze how various control factors, including temperature and membrane thickness, influence the energetic and exergetic efficiencies of the PEM electrolyzer. The model takes into account the phenomenon of water transfer through the membrane. Numerical analysis showed an energetic efficiency of 69.57 % and an exergetic efficiency of 68.08 % under maximum temperature and minimum membrane thickness conditions. Dang et al. [14] utilized a VOF approach to study the bubble flow regime within the anode flow field of the PEM electrolyzer. Numerical results show that the bubble flow regime significantly affects the distribution of liquid water and oxygen bubbles along the channel, which plays a significant role in the pressure drop and substantially affects the electrochemical performance. Zhu et al. [15] presented a simulation using MATLAB/Simulink to analyze the hydrogen production efficiency of PEM electrolyzers, considering parameters such as pressure, temperature, and membrane thickness. Their findings revealed that the membrane thickness is the most significant factor influencing hydrogen production efficiency. When the pressure on the cathode side was increased approximately five times, the hydrogen flow rate decreased by 7.4 mL/min. Afshari et al. [16] examined how membrane thickness, temperature, and cathode pressure affect hydrogen crossover in PEM electrolyzers. They found that most overpotential losses originated from concentration effects, that thicker membranes reduced hydrogen crossover, and that increased cathode pressure enhanced it due to a higher pressure differential. Liao et al. [17] developed several designs of titanium mesh plates and conducted experiments to examine how water conductivity and operating temperature influence the performance of PEM electrolyzers. Their findings revealed that the voltage efficiency was 60.6 % when utilizing a flat Ti-mesh flow field. However, using an embossed Ti-mesh flow field, this efficiency increased to 80.3 %. Lin et al. [18] performed a CFD study on PEM electrolyzer performance using three flow channel structures: parallel, triple-serpentine, and pin. They analyzed pressure and velocity distributions for different channel widths, finding that while the serpentine design offers a higher flow rate than the parallel design, it also results in greater pressure loss. Toghyani et al. [19] developed a numerical model of an electrolyzer operating under varying physical conditions. Their results demonstrated that the hydrogen concentration at the membrane–catalyst interface decreased by approximately 13.64 % as the temperature ranged from its maximum to minimum value. Yan et al. [20] designed a novel flow field with water droplet-shaped ribs for a PEM electrolyzer. Numerical results showed a 0.9 % performance improvement over conventional flow field configurations, mainly because the novel design achieved more uniform distributions of water and temperature. Ozdemir et al. [21] conducted an experimental study investigating the various operational parameters affecting the performance of the PEM electrolyzer. The experimental results indicate that increasing operating temperature improves cell polarization performance and hydrogen production. The experimental results showed that

the energy efficiency achieved was 59.6 %. Xu et al. [22] employed a 3D PEM electrolysis cell stack model with four cells to study temperature distribution, membrane water content, and current density. Their multiphase model considered manifold effects, revealing that the performance of each cell decreases from the first to the last in the water flow direction due to the non-homogeneous distribution of water and heat. Li et al. [23] studied the effects of temperature and pressure on the electrochemical performance of high-temperature PEM electrolyzers, highlighting the importance of maintaining liquid water at high pressures to enhance cell performance. Noor Azam et al. [24] studied the impact of various anode electrocatalysts and operating conditions on the electrochemical performance of PEM electrolyzer and their hydrogen production efficiency. The PEM electrolyzer exhibited optimal performance at a 2 mL/min water flow rate, using an IrRuOx-based anode electrocatalyst at a temperature of 70 °C.

To effectively use proton exchange membrane electrolysis cells (PEMEC) in real-time, developing a predictive capability for their electrochemical performance under various process parameters is essential. In PEM electrolysis technology, multiphase flow, heat transfer, mass transport, and electrochemical reactions are strongly coupled across time and spatial scales. Mathematical modeling of PEM electrolyzer systems offers valuable insights into the complexities of fluid dynamics, species transport, and electrochemical reaction mechanisms. Accurate CFD models provide detailed insights into complex interactions, but they often demand significant computational resources and time, especially for unsteady or large-scale systems. In this context, ML algorithms have emerged as a promising complement to traditional computational fluid dynamics (CFD). ML can reduce computational costs and enable efficient real-time optimization and control by providing rapid and accurate predictions from existing data.

Machine learning (ML) has become a powerful tool for addressing challenges in modeling the electrochemical performance of PEM electrolyzers. ML algorithms excel at identifying complex nonlinear relationships between input variables and output targets, making them beneficial for systems like PEMWE, where multiple interdependent factors influence electrolyzer performance. Machine learning techniques enable accurate predictions from existing data, reducing the computational load and solution time required for computational fluid dynamics (CFD) analyses and promoting more efficient optimization.

Although machine learning applications in PEMWE systems remain limited, several studies in this direction have emerged in the literature over the past few years, some of which are summarized below.

Madhavan et al. [25] introduced machine learning techniques to predict the corrosion characteristics of PTL coatings with different alloy compositions in PEM water electrolyzers. The dataset was split into two parts: one aimed at forecasting corrosion current density and the other at estimating end-of-life voltage. They developed models using extreme gradient boosting and Artificial Neural Networks (ANN). The ANN model, using mean squared error as the loss function, achieved an R^2 value of 0.993 for corrosion current density. Moreover, the ANN model using the mean squared error loss function caused an R^2 of 0.966 for end-of-life voltage estimations, surpassing the XGB models. Ozdemir and Pektezel [26] have utilized experimental data from a proton exchange membrane water electrolyzer system to predict current density and hydrogen flow rate using MLP, SVM, and RF algorithms. The dataset included cell voltage, temperature, torque, and water flow rate as inputs. The results demonstrated that the SVM method outperformed the other methods in terms of prediction accuracy, with current density predicted with an MAE of 0.0371 and hydrogen flow rate predicted with an MAE of 0.0671 on the test set. Hayatzadeh et al. [27] applied machine learning techniques to experimental data extracted from a commercial PEM water electrolyzer to investigate the influence of various factors, including operating temperature and current density. They employed support vector regression (SVR) and ANN techniques for this analysis. The results demonstrated that SVR, when its hyperparameters were optimized with a genetic algorithm (GA), could accomplish an estimation performance similar to that of an ANN with a fully connected structure, featuring two hidden layers, each containing 30 neurons. Shomope et al. [28] applied three machine learning techniques—random forest (RF), support vector machine (SVM), and extreme gradient boosting (XGBoost)—to forecast hydrogen production in PEMWE. The best models, RF and XGBoost, were fine-tuned through hyperparameter optimization. The RF model delivered a predictive performance with $R^2 = 0.9898$, RMSE = 19.99 mL/min, and MAE = 10.41 mL/min, whereas the XGBoost model performed $R^2 = 0.9894$, RMSE = 20.43 mL/min, and MAE = 11.50 mL/min. Tawalbeh et al. [29] developed an ANN model to accurately estimate the hydrogen production rate in PEMWE systems. The model utilizes key operational variables such as anode and cathode surface areas, cell voltage, current, water flow rate, power, and temperature as input features. The results demonstrated that the ANN model substantially outperformed conventional approaches, accomplishing an R^2 value of 0.9989 and an MAE of 0.012. In contrast, models based on RF ($R^2 = 0.9795$), linear regression ($R^2 = 0.9697$), and SVM ($R^2 = 0.4812$) exhibited lower predictive performance, highlighting the superiority of the ANN-based approach.

In this study, four machine learning algorithms—Support Vector Machine (SVM), ElasticNet, M5P, and Multilayer Perceptron (MLP)—were utilized to predict current density in a computational fluid dynamics (CFD) model of a PEM electrolyzer. SVM is well-known for its effectiveness in handling high-dimensional regression problems, especially when the data exhibits non-linear relationships. Given that the CFD-derived current density may involve such nonlinearities, SVM was included to evaluate its ability to model these patterns. MLP was selected to assess how well a non-linear, feed-forward neural network could capture the complex relationships in the dataset. M5P provides both interpretability and flexibility by breaking the problem into subspaces and fitting linear models. This dual nature made it a suitable candidate for both accuracy and model transparency. Elastic Net was chosen to represent linear regression models with embedded feature selection. Its ability to handle multicollinearity and perform variable selection is advantageous when dealing with potentially correlated inputs derived from CFD simulations. The intention was to cover a balanced range of ML paradigms (kernel-based, neural network-based, tree-based, and regularized regression), rather than exhaustively testing all available algorithms. A full-scale, three-dimensional, multiphase CFD model was developed to examine the electrochemical performance of the PEM electrolyzer. The input variables considered included cell voltage, temperature, membrane thickness, and the porous transport layer's (PTL) thickness. The results from the CFD model were analyzed using ML techniques to uncover meaningful patterns and correlations related to system performance. A review of existing literature reveals that the application of artificial intelligence and machine learning in PEM electrolyzer systems is still limited and underexplored. There is a significant need for comprehensive studies that assess the effectiveness of various ML algorithms in enhancing electrolyzer system performance. This study contributes novel insights by integrating the analysis of a detailed 3D, multi-phase CFD model of a PEM electrolyzer with machine learning methods, thereby providing new understanding of the complex interactions affecting system performance.

2. CFD model development

The PEMEL includes an anode current collector (ACC), a cathode current collector (CCC), an anode flow channel (AFC), a cathode flow channel (CFC), an anode porous transport layer (APTL), a cathode porous transport layer (CPTL), and a membrane electrode assembly (MEA). In a PEMEL, the MEA serves as the core of the cell, with the polymer membrane positioned between the porous transport layers on both the anode and cathode sides. Deionized water flows into the anode side through a channel and is electrochemically separated into hydrogen ions and oxygen using electrical energy. Anodic, cathodic, and overall reactions in PEM water electrolysis technology can be summarized as

Table 1
Governing equations [31].

Physical process	*Governing equation*	*Description*
Continuity	$\nabla \bullet \vec{u} = 0$	$\vec{u}$ is the velocity field
Navier-Stokes	$\rho(\vec{u} \bullet \nabla)\vec{u} = -\nabla P + \mu\nabla^2\vec{u} + \vec{F}$	$\vec{F}$ is the body force
Energy	$\rho c_p(\vec{u} \bullet \nabla T) = \nabla \bullet (k\nabla T) + Q_{gen}$	Q_{gen} is the total heat generation
Total heat generation	$Q_{gen} = i_{local} \bullet \eta + \frac{i_{local}^2}{\sigma_{eff}}$	where the first term represents heat generated by overpotential, while the second term accounts for Joule heating in conductive domains.
Species Transport	$\vec{u} \bullet \nabla c_i = \nabla \bullet (D_i \nabla c_i) + \frac{R_i}{\rho}$	c is the concentration of species, R_i is the source term
Electric charge	$\nabla \bullet (\sigma_s \nabla \phi_s) = -S_{ct} \nabla \bullet (\sigma_m \nabla \phi_m) = + S_{ct}$	S_{ct} is the charge transfer source term, ϕ_s is the solid phase potential, ϕ_m is the membrane phase potential, σ_s is the electronic conductivity, σ_m is the membrane conductivity
Electrochemical source	$R_i = \alpha_s \bullet i_{local} \bullet \frac{M_i}{n_i \bullet F}$	R_i is the species source term based on the local current density, where α_s is the specific surface area
Local current density	$i_{local} = i_0\left[exp\left(\frac{\alpha_a \bullet F \bullet \eta}{R \bullet T}\right) - exp\left(-\frac{\alpha_c \bullet F \bullet \eta}{R \bullet T}\right)\right]$	Butler-Volmer kinetics governs i_{local}; i_0 is the exchange current density, η is the overpotential, and α_a, α_c are the anodic and cathodic transfer coefficients
Liquid phase volume fraction	$\nabla \bullet (\alpha_w \vec{u}) = 0$	Transport equation for steady-state water volume fraction, where α_w is the liquid phase fraction in the anode flow channel
Gas phase volume fraction	$\alpha_g = 1 - \alpha_w$	α_g is the oxygen gas phase fraction in the anode flow channel

follows [30]:

Anodic side:

$$H_2O \rightarrow 2H^+ + 0.5O_2 + 2e^- \quad (1)$$

Cathodic side:

$$2H^+ + 2e^- \rightarrow H_2 \quad (2)$$

Overall:

$$H_2O \rightarrow H_2 + 0.5O_2 \quad (3)$$

In this study, a steady-state, three-dimensional model has been developed, considering two-phase flow physics within the anode flow channel of the PEMEL. Additionally, the model incorporates critical elements such as continuity, Navier-Stokes equations, energy, chemical species, and electric charge. The governing equations are listed in Table 1. The three-dimensional model geometry and the porous media of PEMEL are illustrated in Fig. 1.

To simplify the numerical model and calculations, the following assumptions have been adopted:

(1) The numerical model was solved under steady-state conditions.
(2) The flow of fluid within the channels and porous layers is considered laminar and incompressible.
(3) It is assumed that the porous layers have a homogeneous and isotropic structure.
(4) The impact of gravity is ignored.
(5) This study investigates a configuration in which water is supplied exclusively to the anode side of the PEMEL, with negligible liquid water transfer to the cathode side through the membrane. This study focuses on the two-phase flow occurring in the anode compartment, specifically analyzing the electrochemical performance of the electrolyzer by incorporating the dynamics of liquid water and oxygen gas bubbles into the numerical model.

ANSYS Fluent CFD software, featuring an integrated Fuel cell and Electrolysis module, has been employed [32]. A hexahedral mesh was utilized, and a comprehensive mesh sensitivity analysis was conducted to assess the effectiveness of the meshing strategy and its resolution. To minimize cutting errors in the numerical solution, a finer mesh was used for the MEA and porous transport layers of the PEMEL. The effect of the number of cells on CFD simulation results is explored to prove that the outcomes remain consistent, regardless of the number of elements used. The five types of meshes were utilized in the PEMEL for mesh sensitivity analysis. To evaluate mesh independence in this study, the volume integral of transfer current within the catalyst layers was selected as the representative parameter. Table 2 presents the data indicating that the difference in transfer current between cell numbers 923,750 and 1,015,625 is measured at 0.828 % at a voltage of 0.7 V. Additionally, the difference in transfer current between cell numbers 1,015,625 and 1,242,621 is recorded at a minimal 0.008 % at the same voltage. A finer mesh increases the computational load, while a coarse mesh decreases the accuracy of the simulation results. To balance the computational load and accuracy, a mesh structure with 1,015,625 cells was used in all simulations, as shown in Fig. 2.

2.1. Boundary conditions and solution approach

The inlet boundary condition for the anode is defined by the water flow rate. Pressure outlet boundary conditions at the anode and cathode outlets are set to atmospheric pressure, with backflow total temperature adjusted to the temperature field setup. The walls were treated with no-slip boundary conditions. The cathode terminals were set to zero volts while varying electric potential values were applied to the anode to generate a polarization curve. A finite volume method is used to solve the CFD model equations, with the SIMPLE scheme implemented as the solution method. The spatial discretization of all governing equations was carried out using a first-order upwind scheme. The Bi-conjugate Gradient Stabilized (BiCGSTAB) method and F-cycle multigrid cycle were employed for all equations to achieve faster convergence in solutions. Under-relaxation factors are adjusted to 0.3, 1, 1, 0.7, 1, 1, and 1 for pressure, density, body forces, momentum, volume fraction, energy, and potential, respectively. The physical parameters and boundary conditions listed in Tables 3 and 4 were used in the CFD analysis.

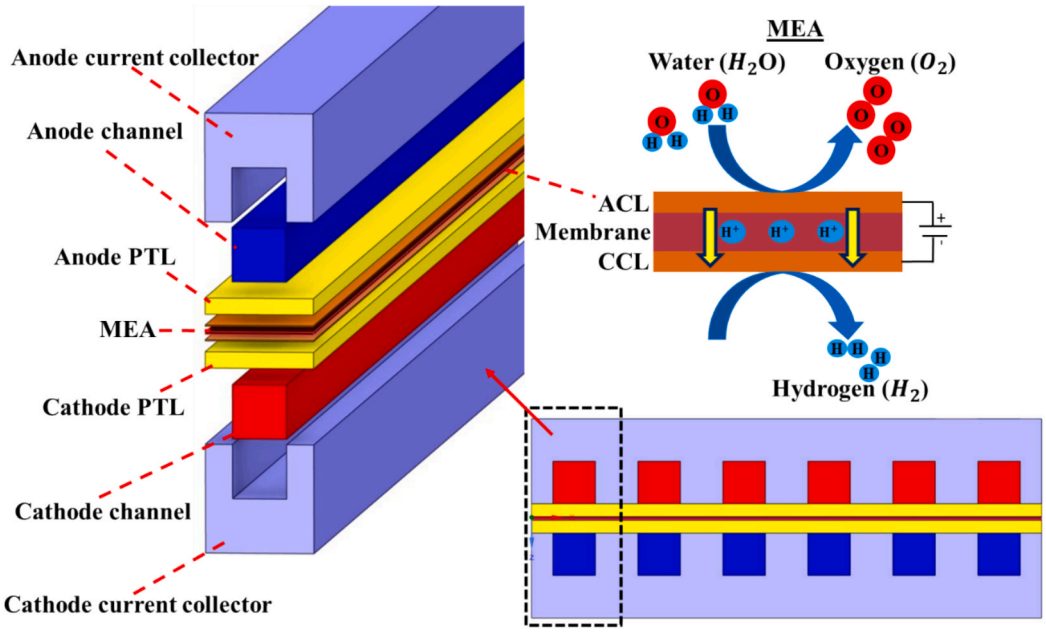

Fig. 1. Schematic illustration of the PEMEL model.

Table 2
Mesh sensitivity analysis.

Mesh Case	*Number of Cells*	*Transfer Current (A)*	*% Difference*
1	62,211	1.1715	–
2	530,000	1.2310	5.079 %
3	923,750	1.2555	1.990 %
4	1,015,625	1.2659	0.828 %
5	1,242,621	1.2660	0.008 %

3. Machine learning approaches

Machine learning, a subfield of artificial intelligence, enables computers to learn from input data and make informed decisions by identifying the relationships between input and output variables to construct predictive functions [33]. Machine learning involves developing general-purpose algorithms that can extract insights from specific datasets without the need for explicitly programmed instructions; rather than coding manually, data is provided to the algorithm, which then constructs its own logic based on the patterns it learns from the data [34]. The mathematical basis of machine learning is grounded in linear algebra, statistical methods, and probability theory [35]. ML models are capable of establishing relationships between input and output variables within a given dataset, which is essential for addressing forecasting problems [36]. The advancement of machine learning and advanced data analysis methods offers a promising alternative to physical and experimental testing, with the potential to lower analysis costs by relying exclusively on operational data [37].

Machine learning has significant potential in supporting PEM water electrolyzer research and development across multiple scales—ranging from materials to full system integration. At the materials scale, ML can be used to analyze vast compositional datasets and predict the optimal ratios or structures of catalyst layers, membranes, and ionomers to enhance performance and durability. At the component level, such as flow fields or bipolar plates, ML models can assist in optimizing geometrical features and material selections to improve mass transport, water management, and electrical conductivity. At the device scale, ML enables prediction of key operational metrics (e.g., current density)

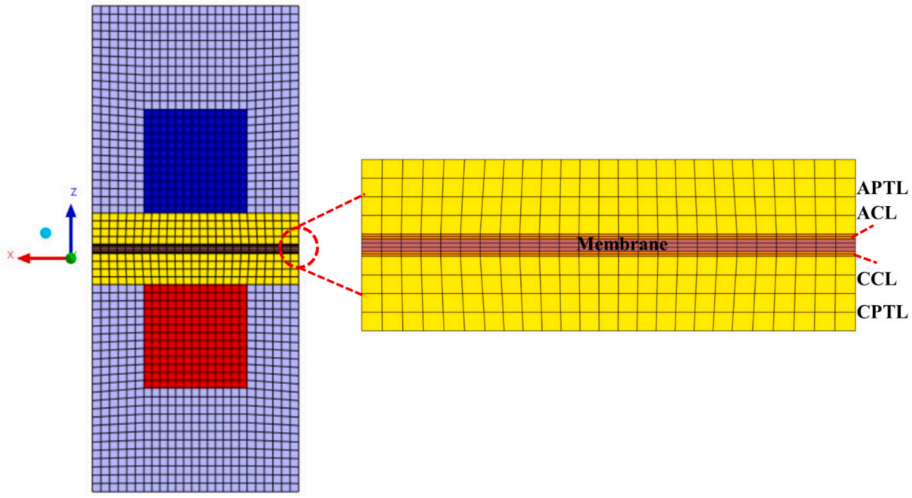

Fig. 2. Mesh resolution.

Table 3
Physical parameters of PEMEL.

Description	*Value*	*Unit*
Width of channel	0.1	cm
Height of channel	0.1	cm
Length of channel	5	cm
CC thickness	1	mm
PTL thickness	100, 200, 300	μm
CL thickness	20	μm
Membrane thickness	25, 50, 100	μm
PTL porosity (ε)	0.5	–
CL porosity (ε)	0.2	–
Membrane porosity (ε)	0.5	–
PTL permeability (K)	1e-12	m^2
Anode CL permeability (K)	4.9e-12	m^2
Cathode CL permeability (K)	2e-12	m^2
Membrane permeability (K)	4.7e-09	m^2
Thermal conductivity of membrane (k)	2	W/mK
Thermal conductivity of CL (k)	10	W/mK
Thermal conductivity of PTL (k)	10	W/mK
Membrane conductivity (σ)	1e-16	S/m
CL conductivity (σ)	5000	S/m
PTL conductivity (σ)	20,000	S/m
Temperature (K)	333.15, 343.15, 353.15	K
Pressure outlet (P_{out})	101,325	Pa
Volumetric flow rate ($\dot{V}$)	300	ml/min
Open circuit voltage	1.1999	V
Active area	50	mm^2

Table 4
Boundary conditions.

Boundary	**Parameter**	**Value/Description**	**Unit**
Anode Inlet	Water flow rate	300	ml/min
	Temperature	333.15–353.15	K
Cathode Outlet	Pressure	101,325	Pa
Channel walls	Velocity	No-slip	–
	Thermal	Adiabatic	–
ACC	Electric potential	1.5–1.725	V
CCC	Electric potential	0	V

Table 5
MLP models.

Model No	*Network Structure*	*Training MAE & RMSE*	*Test MAE & RMSE*
1	4-2-1-1	0.0268 & 0.0315	0.0329 & 0.0392
2	4-2-2-1-1	0.0236 & 0.0294	0.0361 & 0.0465
3	4-3-1-1	0.0278 & 0.0314	0.0366 & 0.0513
4	4-3-3-1-1	0.0256 & 0.0306	0.0378 & 0.0485
5	4-4-1-1	0.0289 & 0.0340	0.0343 & 0.0412
6	4-4-4-1-1	0.0277 & 0.0323	0.0378 & 0.0456
7	4-5-1-1	0.0266 & 0.0321	0.0320 & 0.0405
8	4-5-5-1-1	0.0273 & 0.0337	0.0354 & 0.0428
9	4-6-1-1	0.0249 & 0.0308	0.0363 & 0.0431
10	4-6-6-1-1	0.0271 & 0.0332	0.0353 & 0.0420
11	4-7-1-1	0.0289 & 0.0328	0.0355 & 0.0492
12	4-7-7-1-1	0.0276 & 0.0338	0.0329 & 0.0400
13	4-8-1-1	0.0223 & 0.0286	0.0283 & 0.0374
14	4-8-8-1-1	0.0289 & 0.0347	0.0328 & 0.0394

under varying boundary conditions, as demonstrated in this study. Lastly, at the system scale, ML can contribute to real-time control, and predictive maintenance strategies by analyzing operational trends and providing early warning for anomalies.

3.1. MLP method

MLP is regarded as a fundamental artificial neural network algorithm that mimics the behavior of the human nervous system by utilizing interconnected neurons to process and analyze data. Unlike the single-layer perceptron, the multilayer perceptron consists of several sequentially connected perceptron layers, and its hidden layers enable improved accuracy for data that is not linearly separable [38]. Multi-layer perceptron algorithm offers a dependable and adaptable structure for regression problems by capturing intricate patterns within data and delivering accurate predictions when appropriately configured and trained [39]. The initial component of MLP is the input layer, which enables interaction between the network and its external environment; the second component is the hidden layer, typically consisting of one or more neuron layers depending on the complexity and generalization needs of the task; and the final component is the output layer [40].

Table 6
Hyperparameter optimization for MLP.

Learning Rate	*Momentum*	*Training MAE & RMSE*	*Test MAE & RMSE*
0.2	0.2	0.0261 & 0.0322	0.0315 & 0.0379
0.2	0.25	0.0260 & 0.0325	0.0312 & 0.0377
0.2	0.3	0.0263 & 0.0330	0.0310 & 0.0381
0.3	0.2	0.0223 & 0.0286	0.0283 & 0.0374
0.3	0.25	0.0228 & 0.0289	0.0292 & 0.0386
0.3	0.3	0.0241 & 0.0298	0.0308 & 0.0407
0.4	0.2	0.0227 & 0.0280	0.0289 & 0.0382
0.4	0.25	0.0220 & 0.0272	0.0283 & 0.0374
0.4	0.3	0.0231 & 0.0281	0.0296 & 0.0394

Table 5 presents the various network architectures developed using the MLP method. A total of 14 models were constructed, and the prediction performance of each model was evaluated on both the training and test datasets. The models were designed based on variations in the number of hidden layers and the number of neurons within these layers. Upon examining the results in Table 5, it was observed that Model 13 yielded the lowest error on both the training and test sets, indicating that it is the optimal model. The network architecture of Model 13 follows a 4-8-1-1 configuration.

Table 6 illustrates the hyperparameter optimization process conducted for the MLP method. This optimization was performed using the 4-8-1-1 network architecture, which was identified as the optimal configuration based on the performance evaluation of various network models. In this context, the learning rate and momentum were systematically varied within specific ranges to optimize the MLP model and reduce prediction error. Upon reviewing the results presented in Table 6, the optimal learning rate was determined to be 0.4, and the optimal momentum was found to be 0.25, as these values yielded the lowest prediction error on both the training and test datasets.

Fig. 3 depicts the network architecture of the optimal MLP model, which follows the 4-8-1-1 configuration. In this model, cell voltage, temperature, membrane thickness, and PTL thickness are used as input parameters, while the output parameter is current density.

MLP is capable of approximating complex functions, making it suitable for modeling intricate CFD relationships. Effectiveness of MLP was evaluated in terms of predictive accuracy (RMSE, MAE, R^2, a20-index), and model sensitivity to learning rate and momentum. It generally required longer training time due to backpropagation but provided high accuracy in most cases. Its computational resources were moderate to high depending on architecture depth and training iterations. Practical application of MLP is that it is suitable for problems with nonlinearity, such as current density prediction in electrochemical systems.

3.2. M5P method

The M5P algorithm is an extended form of the original M5 model introduced by Quinlan [41]. The M5 tree is a sophisticated decision tree model known for its efficiency and accuracy in high-dimensional regression applications, with the M5P version formatted as a binary regression structure in which the terminal leaves apply linear regression equations to yield continuous numerical predictions [42]. Owing to its resilience in handling incomplete data and its capacity to deliver

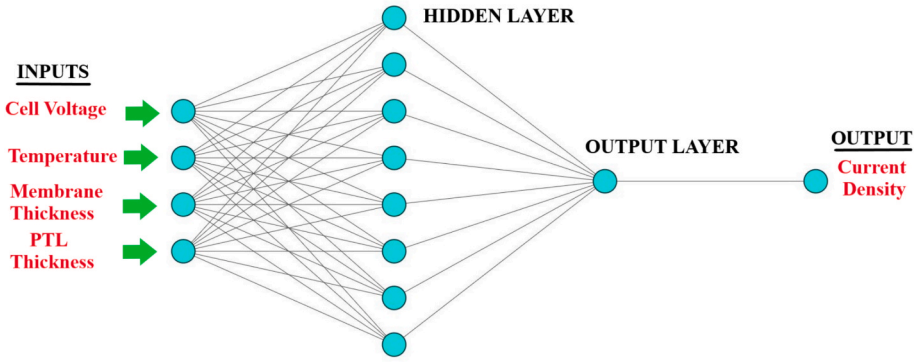

Fig. 3. MLP network sequence.

Table 7
M5P hyperparameter optimization.

Model No	*Minimum Number of Instances per Leaf*	*Pruning*	*Training MAE & RMSE*	*Test MAE & RMSE*
1	1	Yes	0.0493 & 0.0619	0.0647 & 0.0735
2	1	No	0.0464 & 0.0581	0.0574 & 0.0670
3	10	Yes	0.0782 & 0.0993	0.1076 & 0.1318
4	10	No	0.0604 & 0.0816	0.0980 & 0.1220
5	20	Yes	0.0642 & 0.0861	0.1017 & 0.1224
6	20	No	0.0643 & 0.0848	0.1012 & 0.1286

interpretable equations linking input and output variables, the M5 algorithm has been applied to various engineering challenges [43].

The construction of the tree is carried out using standard deviation reduction, which aims to reduce the anticipated prediction error at each node and is expressed by Equation 4. In this equation, sd denotes the standard deviation, S refers to the data instances, and S_i represents the subsets resulting from the node split based on the selected attribute.

$$\text{Standard Deviation Reduction} = \text{sd}(S)\text{-}\sum_i \frac{S_i}{|S|} \times \text{sd}(S_i) \tag{4}$$

Table 7 presents the hyperparameter optimization process conducted for the M5P method. In the models developed for this purpose, two variables were considered. The first variable, the minimum number of instances per leaf, determines the minimum number of samples required at each leaf node of the model. A smaller value may lead to increased branching, resulting in a more complex model, while a larger value tends to produce a simpler structure. The second variable involves the decision of whether pruning is applied. Pruning restricts the growth of the decision tree. Selecting 'Yes' leads to a more simplified model by avoiding unnecessary branches, whereas selecting 'No' allows for a deeper and more complex model structure. Based on the results presented in Table 7, it can be concluded that Model 2 is the optimal model, as it yields the lowest error on both the training and test datasets. In Model 2, the minimum number of instances per leaf parameter was set to 1, and pruning was disabled (set to No), leading to the best predictive performance with minimal error.

M5P offers interpretability through tree structure and linear regression leaves, enabling an analytical understanding of model behavior. Effectiveness of M5P includes balanced performance with fast computation and moderate accuracy. Also, it is useful for identifying local linear trends within the CFD results. M5P is a suitable candidate for applications where both accuracy and model transparency are required.

Table 8
ElasticNet hyperparameter optimization.

Model No	*Alpha*	*Training MAE & RMSE*	*Test MAE & RMSE*
1	0.1	0.1799 & 0.1991	0.1529 & 0.1808
2	0.3	0.0905 & 0.1017	0.0787 & 0.0985
3	0.5	0.0703 & 0.0835	0.0742 & 0.0971
4	0.7	0.0627 & 0.0786	0.0732 & 0.0946
5	0.9	0.0591 & 0.0774	0.0715 & 0.0927

3.3. ElasticNet method

Elastic Net is a regularization technique for linear regression that simultaneously conducts variable selection [44]. Ridge and Lasso regression solutions are integrated to construct the optimal model; hence, ElasticNet Regression represents a hybrid of Ridge and Lasso techniques [45]. Ridge regression relies on squared values for regularization, while Lasso regression employs absolute values; ElasticNet combines these two biased estimation techniques into a unified modeling approach [46]. The advantage of ElasticNet lies in its ability to perform feature selection, which Ridge regression lacks, while also enabling feature grouping, a limitation of Lasso regression [47].

ElasticNet regression solves the problem defined in Equation (5).

$$\min_\beta \left[\frac{1}{2n} \left(\sum_{i=1}^{n} \left(y_i\text{-}x_i^T\beta\right)^2 + [\text{GSLL}]P_\alpha(\beta) \right) \right] \tag{5}$$

where penalty is defined with Equation (6).

$$P_\alpha(\beta) = (1\text{-}\alpha)\frac{1}{2}\|\beta\|_{l_2}^2 + \alpha\|\beta\|_{l_1} \tag{6}$$

In Equations (5) and (6), β is the regression vector, α corresponds to the elasticity parameter, λ defines the regularization parameter l_1 and l_2 are the norms [48]. When α equals 0, ElasticNet corresponds to Ridge regression, and when α equals 1, it becomes Lasso regression; therefore, ElasticNet determines the optimal α value within the interval 0 and 1 [49]. Table 8 presents the hyperparameter optimization process performed for the ElasticNet regression model. The models were generated by varying the Alpha parameter over a range of values. Setting Alpha to 0 corresponds to Ridge regression, while setting it to 1 corresponds to Lasso regression. For ElasticNet, Alpha was varied between 0 and 1, as the method combines both Lasso and Ridge regression techniques. While the Alpha parameter was adjusted, the Lambda parameter was kept at its default value, as altering Lambda resulted in a significant increase in prediction error compared to the default setting, thereby reducing model performance. An examination of the results in Table 8 reveals that the lowest error on both the training and test datasets was achieved when the Alpha parameter was set to 0.9.

Elastic Net was selected because it represents regularized linear models with embedded feature selection, ideal for checking linear trends

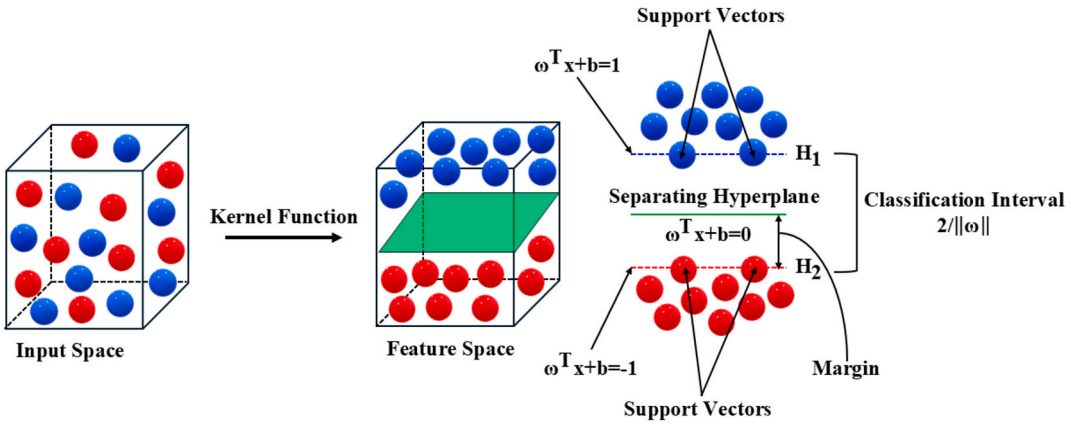

Fig. 4. SVM operation mechanism.

Table 9
SVM models.

Model No	*Kernel Function*	*Training MAE & RMSE*	*Test MAE & RMSE*
1	Normalized Polynomial Kernel	0.1763 & 0.2180	0.1954 & 0.2435
2	Polynomial Kernel	0.0522 & 0.0894	0.0801 & 0.1166
3	Pearson VII (PUK) Kernel	0.0032 & 0.0050	0.0459 & 0.0803
4	Radial Basis Function Kernel	0.3473 & 0.3875	0.3264 & 0.3586

Table 10
SVM hyperparameter optimization.

Hyperparameter	*Value*	*Training MAE & RMSE*	*Test MAE & RMSE*
	2	0.0066 & 0.0098	0.0481 & 0.0848
	2.5	0.0054 & 0.0086	0.0475 & 0.0825
C	3	0.0045 & 0.0076	0.0464 & 0.0812
	3.5	0.0034 & 0.0062	0.0452 & 0.0799
	4	0.0029 & 0.0051	0.0444 & 0.0787
	4.5	0.0023 & 0.0033	0.0421 & 0.0774
	5	0.0032 & 0.0042	0.0437 & 0.0792
	0.5	0.0149 & 0.0196	0.0676 & 0.0980
	1	0.0123 & 0.0175	0.0421 & 0.0774
Sigma	1.5	0.0092 & 0.0154	0.0273 & 0.0543
	2	0.0081 & 0.0137	0.0215 & 0.0405
	2.5	0.0068 & 0.0108	0.0202 & 0.0371
	3	0.0137 & 0.0171	0.0283 & 0.0446
	3.5	0.0173 & 0.0211	0.0374 & 0.0511

and reducing overfitting in presence of multicollinearity. Its effectiveness can be evaluated by taking into account its lower accuracy compared to nonlinear models but fast computation and stability. The practical application of Elastic Net is that it serves as a baseline linear regression model and helps in identifying the presence or absence of linear structure in the CFD-derived data.

3.4. SVM method

The principle of support vector machines, introduced by Vapnik, is based on statistical learning theory, offers high performance, and operates as a supervised machine learning method. SVM is a robust machine learning algorithm capable of precisely estimating response values in complex systems [50]. SVM has been widely utilized in tasks such as classification, regression, and prediction. SVM has the ability to capture nonlinear relationships among data. Compared to conventional machine learning methods, SVM follows the structural risk minimization principle, which aims to reduce the maximum possible generalization error rather than merely decreasing the training error [51].

Fig. 4 explains the working mechanism of the SVM method. The two parallel hyperplanes containing the support vectors are denoted as H_1 and H_2 with the dashed lines. The samples composed of two-class are represented by blue and red spheres, and the support vectors are the data points lying on the dashed lines. The margin refers to the distance between each dashed line and the central separating hyperplane. The classification interval, equal to $2/\|\omega\|$, represents the distance between H_1 and H_2, where $\|\omega\|$ denotes the norm. The separating hyperplane is defined by Equation (7), where ω is the vector orthogonal to the hyperplane, x represents a data instance lying on the hyperplane, and b denotes the bias term.

$$\omega^{T}x + b = 0 \tag{7}$$

In the working principle of SVM, the input space is transformed into the feature space using a Kernel function, where an optimal separating hyperplane is constructed. The main goal of SVM is to identify the best hyperplane that separates data points belonging to different classes. SVM employs a mathematical optimization process to determine the optimal hyperplane in the transformed feature space. The selection of the Kernel function greatly influences the performance of the SVM algorithm, and the most suitable Kernel varies depending on the specific properties of the dataset.

Table 9 presents the models developed using the SVM method. Four different kernel functions were employed: Normalized Polynomial Kernel, Polynomial Kernel, Pearson VII (PUK) Kernel, and Radial Basis Function Kernel. An analysis of the results in Table 9 indicates that the Pearson VII (PUK) Kernel, represented by Model 3, predicted current density with lower error than the other models on both the training and test datasets, and was therefore selected as the optimal model. This function is represented by Equation (8) [52]. In this equation, x_i and x_j are used to express the vector arguments, Pearson half-width is defined with σ, and w symbolizes the peak tailing factor.

$$K(x_i x_j) = \frac{1}{\left[1 + \left(\frac{\sqrt[2]{\|x_i - x_j\|^2 \sqrt{2^{(1/w)}-1}}}{\sigma}\right)^2\right]^w} \tag{8}$$

Table 10 presents the hyperparameter optimization process for the SVM method. The Pearson VII (PUK) kernel function was employed during the optimization phase, as it demonstrated lower prediction error compared to the other kernel types. The hyperparameters C and Sigma were systematically varied within specific ranges to minimize prediction error. Initially, with Sigma set to its default value, the C parameter was varied between 2 and 5. It was observed that a C value of 4.5 resulted in

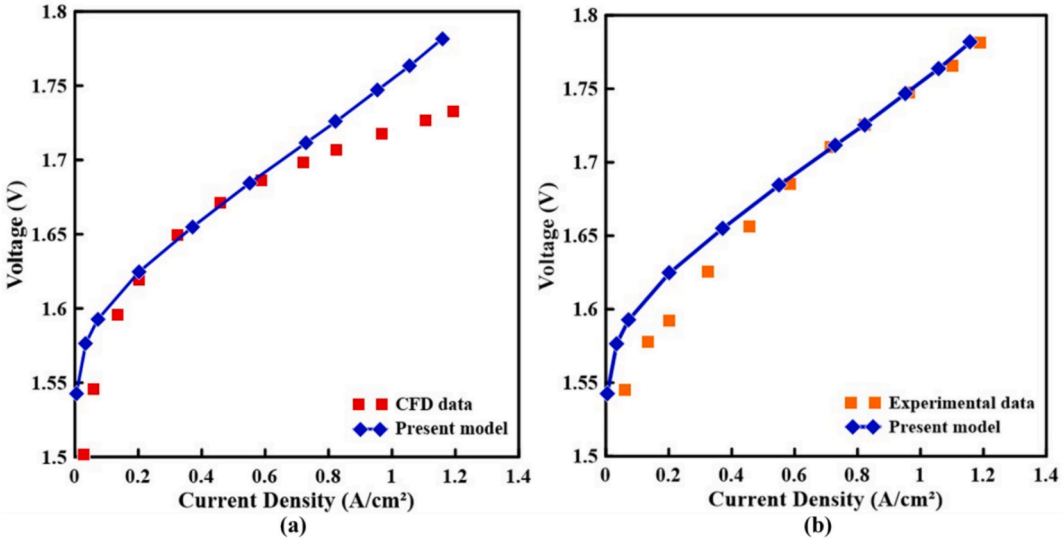

Fig. 5. Model validation with CFD data (a) and experimental data (b).

the lowest error on both the training and test datasets, and thus C = 4.5 was selected as the optimal value. Subsequently, keeping C fixed at 4.5, the Sigma parameter was varied between 0.5 and 3.5. The results indicate that the lowest error occurred when Sigma was set to 2.5, suggesting that Sigma = 2.5 is the optimal value.

SVM is known for robustness and effectiveness in high-dimensional, nonlinear problems. The use of the PUK Kernel enhanced its flexibility. Its effectiveness can be defined with high accuracy and low sensitivity to overfitting, particularly with well-tuned C and sigma parameters. Computational time of SVM is fast during prediction. SVM's practically applicable structure makes it effective in cases with complex boundaries and nonlinear trends, as encountered in CFD data.

In this study, hyperparameter optimization was performed manually using the WEKA interface. Instead of automated techniques such as GridSearchCV, RandomizedSearchCV, or Bayesian optimization, the key hyperparameters for each algorithm were systematically varied and tested one by one. The selection of this manual approach was based on certain considerations. Given the relatively limited dataset size and the small number of models under consideration, exhaustive automated search methods were not computationally necessary. Manual tuning allowed for sufficient exploration of the parameter space. Since WEKA was the primary platform used for model training and evaluation, and its graphical interface is well-suited for controlled manual parameter adjustment, this approach was adopted to ensure consistent experimental design and transparent evaluation [53]. For each algorithm, key hyperparameters known to significantly affect performance were selected and manually varied. While manual tuning is time-consuming, it allowed for a focused and interpretable optimization process aligned with the study's scope.

The effectiveness of each algorithm was defined based on a combination of prediction accuracy via performance metrics (R2, RMSE, MAE, a20-index), model robustness: sensitivity to parameter changes and generalization to unseen data, computational efficiency: training and prediction time, and interpretability: ease of understanding the model's internal behavior. This multi-criteria evaluation allowed for a fair and practical comparison between fundamentally different ML paradigms, each providing complementary insights into the current density prediction task.

4. Results

The findings obtained in this study were examined under two main sections: CFD analysis results and machine learning results.

4.1. CFD analysis results

In this study, a 3D CFD model was developed using ANSYS Fluent software to investigate how physical parameters affect the performance of the PEMEL, particularly its current density. The parameters examined include membrane thickness, PTL thickness, temperature, and cell voltage. The simulation model was designed to encompass mass transport, electrochemical reactions, and proton conductivity within the porous medium. During the parametric analysis, each simulation focused on changing only one physical parameter at a time, while keeping all other parameters constant for comparative analysis. The comprehensive CFD data obtained through this systematic approach was subsequently used to train ML algorithms. The goal was to reliably and rapidly predict the performance of the PEMEL by combining physics-based modeling with data-driven prediction methods.

Fig. 5 demonstrates that the polarization curve derived from the numerical analysis of the PEMEL model closely aligns with both experimental and existing numerical data in the literature. Fig. 5(a) compares the CFD model developed in this study with an existing numerical model from the literature [19]. At low current densities, the results from both models closely align. However, as the current density increases, the differences between the models become more pronounced, leading to a greater mismatch. This discrepancy is primarily because the numerical model referenced was solved using a single-phase flow approach. The primary differences between the present simulation and the model developed by Toghyani et al. [19] concern the treatment of electrochemical reactions and the flow regime assumptions. In the referenced study, user-defined functions (UDFs) were implemented to define electrochemical source terms explicitly, allowing for a customized representation of the reaction mechanisms. In contrast, the present model relies on the built-in electrochemical modules provided by the CFD software, which simplifies implementation but may limit flexibility. Another critical distinction lies in the flow modeling approach: Toghyani et al. [19] employed a single-phase flow model, potentially affecting the accuracy of overpotential predictions due to the absence of phase interaction effects. In the current study, however, a multiphase mixture model is adopted, where the volumetric transfer current is coupled directly with the gas–liquid interactions, offering a more realistic depiction of two-phase flow behavior and its influence on electrochemical performance.

Fig. 5(b) compares the current model, which was validated using experimental data from Debe et al. [54], where the water flow rate, operating temperature, and pressure outlet were 300 ml/min, 360.65 K,

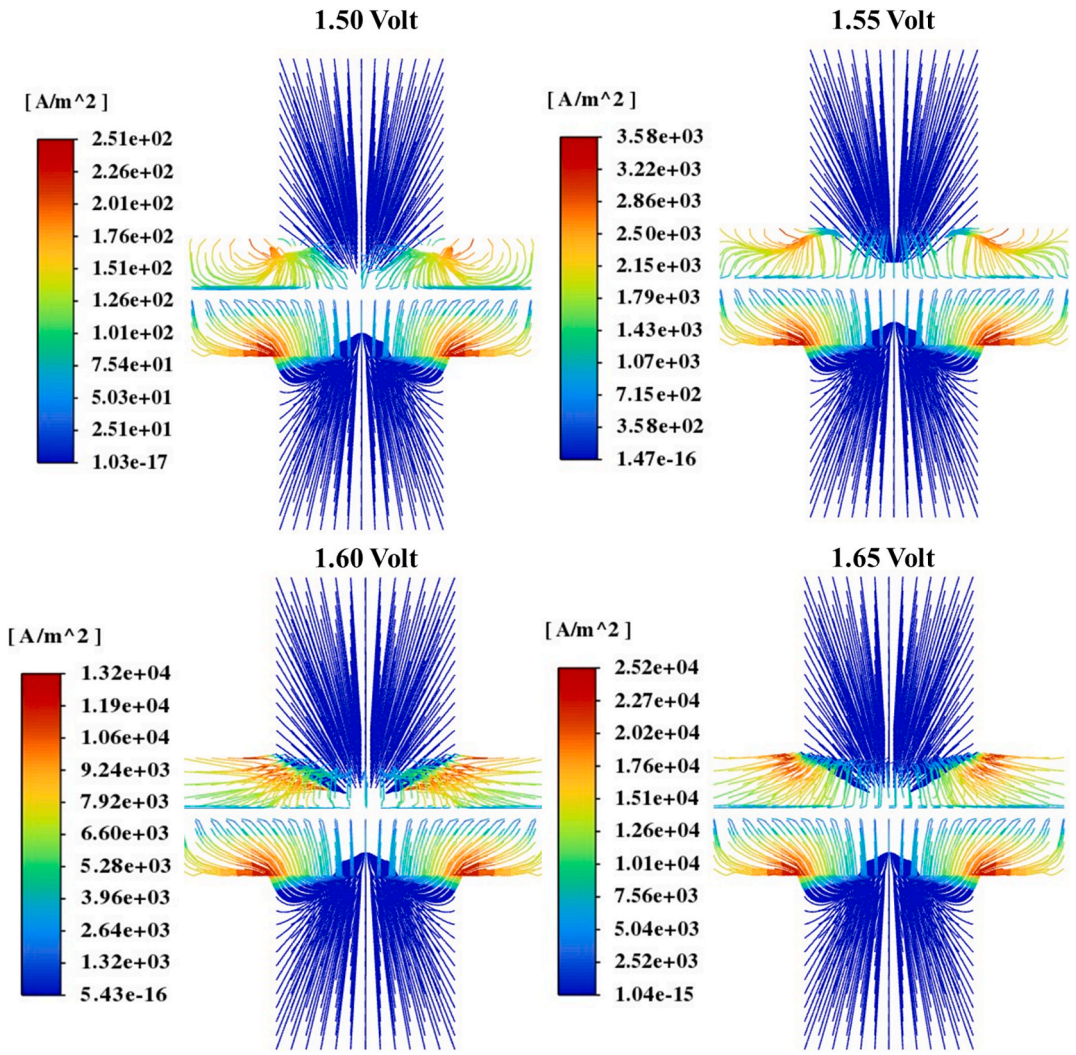

Fig. 6. Current density vector distributions in the PEMEL at different cell voltages.

and 3.954 bar, respectively. For the second comparison, the boundary conditions were defined to match the experimental settings reported by Debe et al. [54]. Specifically, a liquid water flow rate of 300 mL/min and an operating temperature of 360.65 K were prescribed. Since the reported temperature varied between 353.15 K and 368.15 K during measurements, an average temperature was used for the simulations. The total cell voltage applied ranged from 1.498 V to 1.765 V, while the experimental pressure varied between 1.01 bar and 6.89 bar. An average

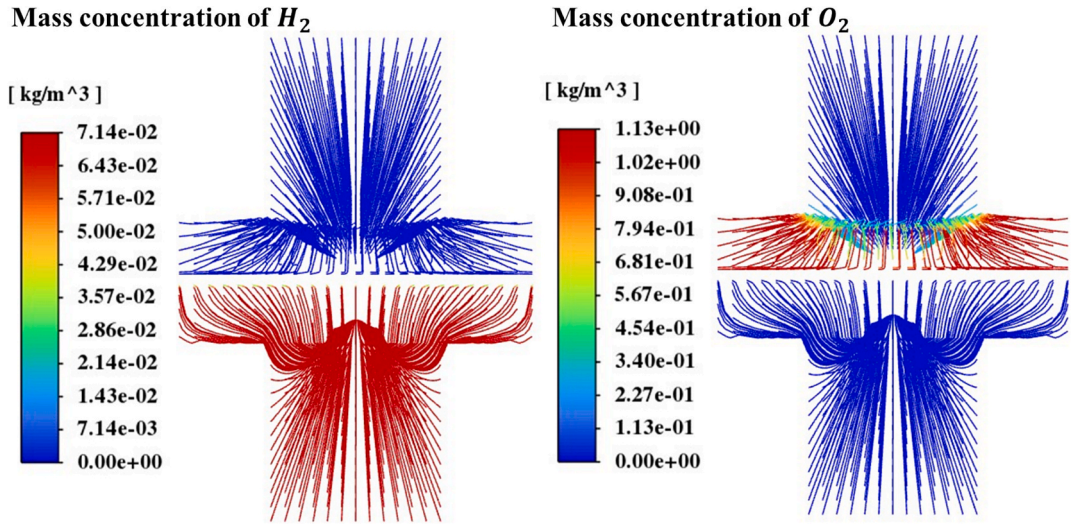

Fig. 7. Mass concentration distributions of hydrogen and oxygen in the PEM electrolyzer for a cell voltage of 1.65 V.

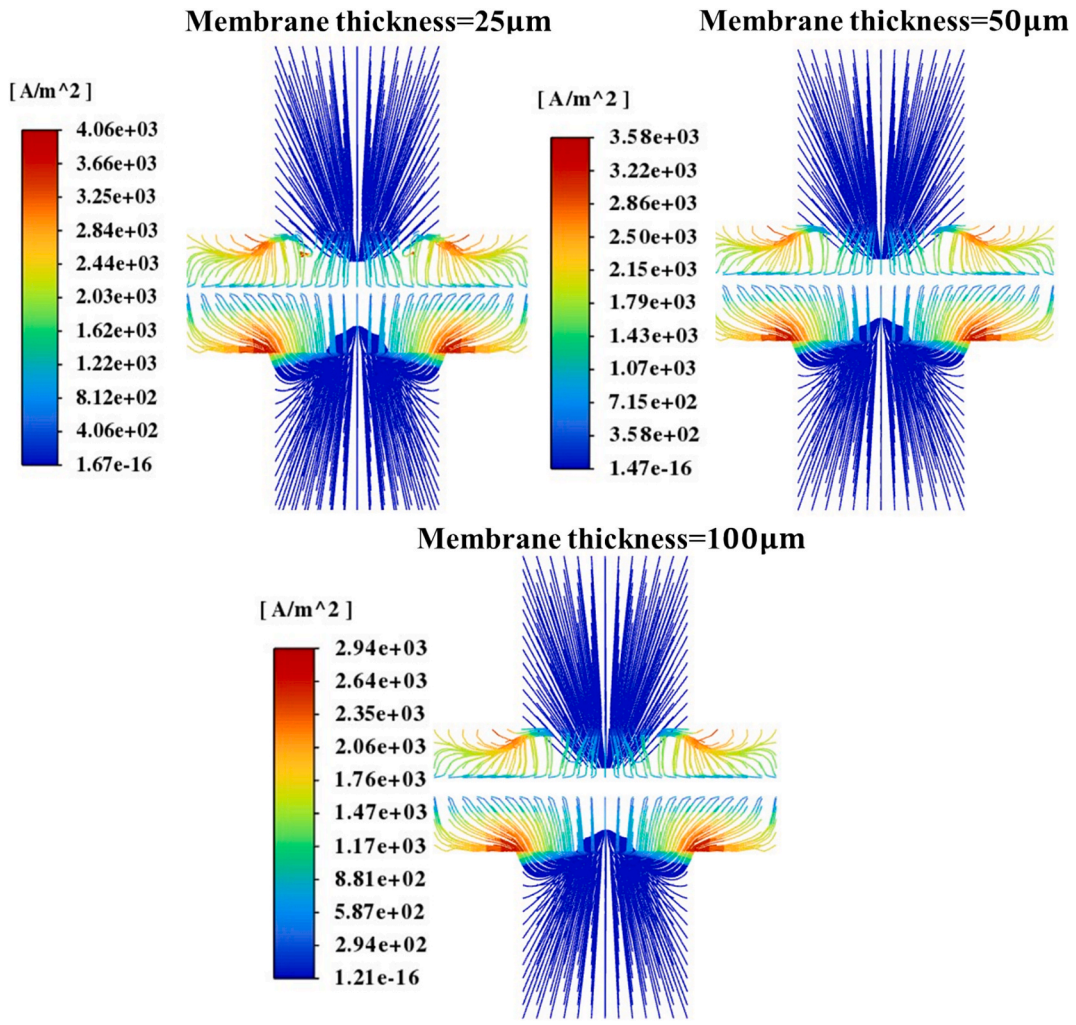

Fig. 8. Current density vector distributions in the PEMEL at different membrane thicknesses.

outlet pressure of 3.954 bar was set as the pressure boundary condition in the numerical model.

Numerical simulations were conducted at a temperature of 343.15 K with a PTL thickness of 300 µm and a membrane thickness of 50 µm to assess how the local current density distribution in the PEMEL is influenced by cell voltage. Their results are displayed as current density vector isosurface plots from the y-axis for different cell voltages: 1.50 V, 1.55 V, 1.60 V, and 1.65 V, as shown in Fig. 6. As the cell voltage increases, there is a noticeable rise in current density, particularly across the MEA. At a cell voltage of 1.50 V, the current density is relatively low and localized. However, when the voltage reaches 1.65 V, the maximum current density exceeds 2.5 A/cm^2, indicating a significant increase in the electrochemical reaction rate. The symmetric and uniform current density distribution indicates a well-constructed numerical model with a high-quality mesh and appropriate boundary conditions.

Fig. 7 shows the transport mechanism of the reaction products resulting from water electrolysis. Numerical simulations were performed at a temperature of 343.15 K, with a cell voltage of 1.65 V, utilizing a PTL thickness of 300 µm and a membrane thickness of 50 µm. Oxygen gas was generated in the anode compartment, while hydrogen gas was produced in the cathode compartment of the CFD model. The simulation results show that the hydrogen mass concentration reaches a maximum of 0.0714 kg/m^3, while the concentration of oxygen peaks at 1.13 kg/m^3. The higher oxygen mass concentration than hydrogen can be attributed to its greater molecular weight. The pathlines are directed from the reaction zone, specifically, the membrane-catalyst interface, toward the cathode gas channel, indicating the outward transport of hydrogen. This flow direction also shows that the oxygen produced by the electrochemical reaction stays on the anode side and is discharged without crossing the membrane.

The impact of three different membrane thicknesses (25 µm, 50 µm, and 100 µm) on the current density distribution is compared in Fig. 8 for a cell voltage of 1.55 V. The chosen operating temperature is 343.15 K, and the thickness of the PTL is 300 µm. As the membrane thickness decreases, the current density increases. The maximum current density of 0.406 A/cm^2 is achieved with the thinnest membrane. Thinner membranes reduce internal resistance, which enhances the electrochemical performance of the PEMEL. Reducing the membrane thickness from 100 µm to 25 µm resulted in an approximately 38 % increase in the maximum current density observed in the MEA region of the PEMEL. However, as the membrane thickness decreases, it is crucial to consider gas crossover and membrane strength parameters. Establishing the optimal membrane thickness guarantees a balance between performance and durability, allowing the system to function efficiently and reliably.

Fig. 9 displays the volume fraction of water distributions within the PEMEL at a cell temperature of 343.15 K and different cell voltages of 1.50 V, 1.60 V, and 1.70 V. The CFD model features a membrane thickness of 50 µm and a PTL thickness of 300 µm. The vector fields depict the flow behavior of the gas–liquid two-phase mixture. At the same time, the color contours show the spatial variation of the water volume fraction across the anode and cathode domains. As the cell

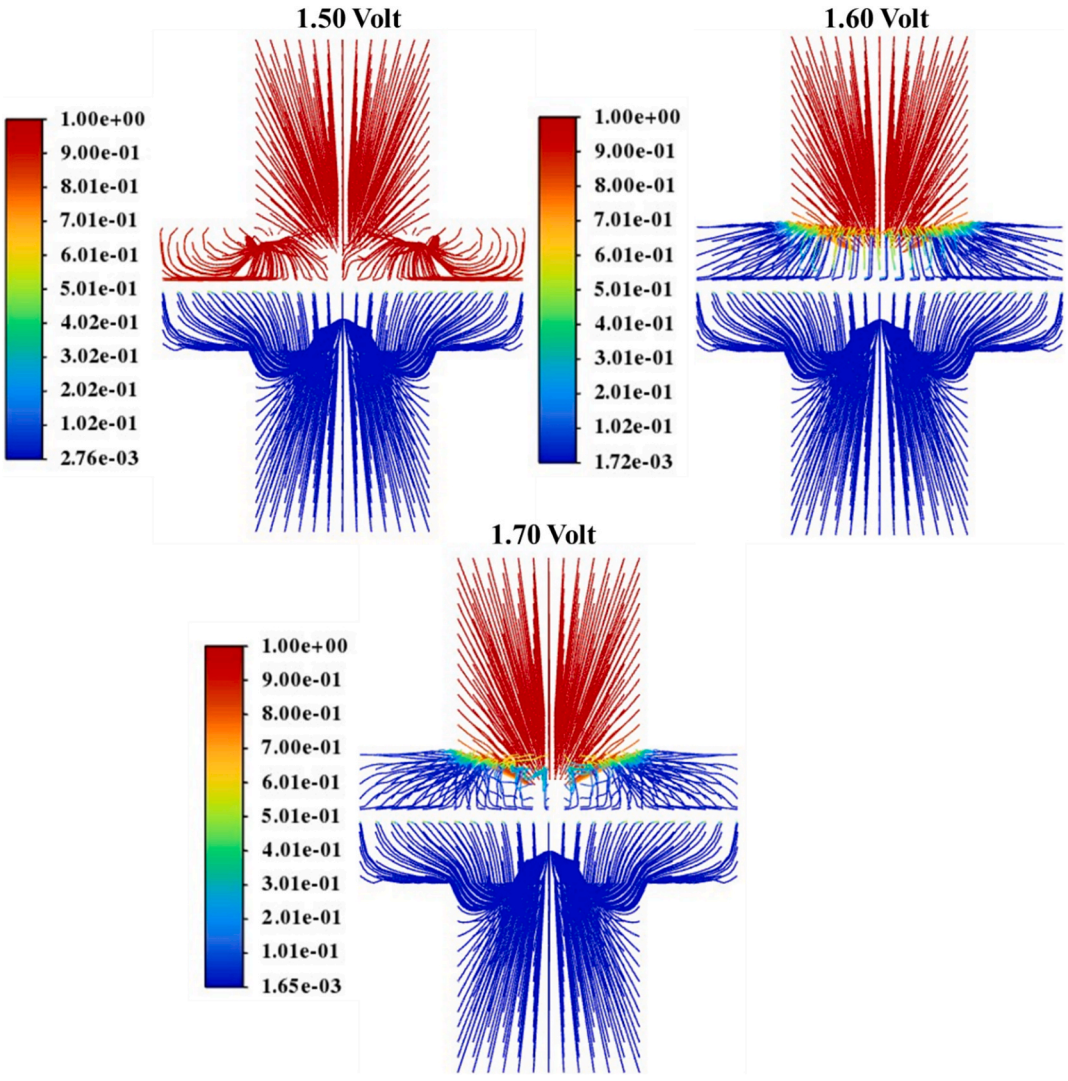

Fig. 9. Volume fraction of water distributions in the PEMEL at different cell voltages and a temperature of 343.15 K.

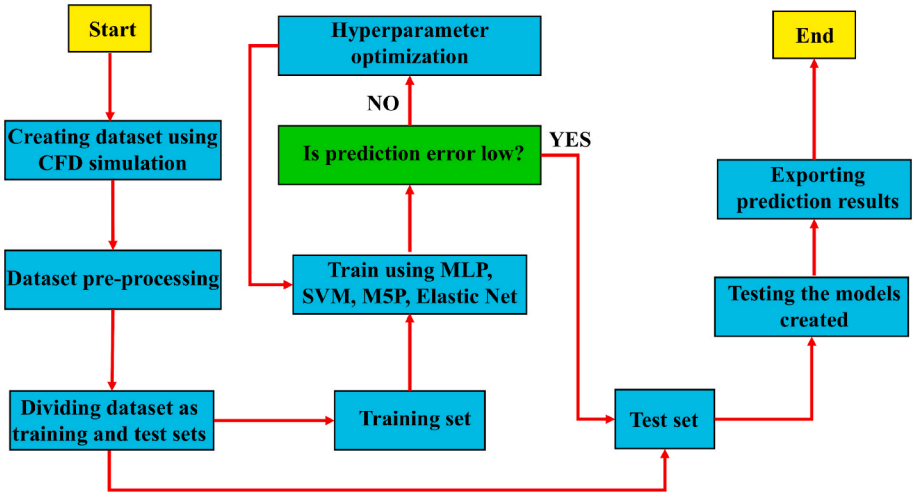

Fig. 10. Machine learning application flow chart.

voltage increases from 1.50 V to 1.70 V, there is a noticeable decrease in the water volume fraction, especially near the membrane interface. This reduction is attributed to the accelerated electrochemical reaction rate and increased hydrogen evolution, which consume more water and promote liquid displacement through the porous media.

Table 11
Statistical summary of the main dataset.

Variable	*Statistical Information*			
	Mean	*Standard Deviation*	*Minimum*	*Maximum*
Cell Voltage (V)	1.61	0.07	1.5	1.73
Temperature (K)	343.15	5.38	333.15	353.15
Membrane Thickness (micron)	53.57	20.98	25	100
PTL Thickness (micron)	257.14	73.37	100	300
Current Density (A/cm^2)	0.65	0.51	0.009	1.582

4.2. Machine learning results

Fig. 10 shows machine learning application procedure. In this study, the WEKA software was utilized for current density prediction processes based on machine learning. SVM, MLP, M5P, and ElasticNet methods were employed for prediction, with the primary motivation for selecting these techniques being their ability to capture non-linear relationships within the dataset. In the dataset, cell voltage, temperature, membrane thickness, and PTL thickness were used as input parameters, while current density was the output parameter, i.e., the target to be predicted. The data required for machine learning were obtained through CFD analyses conducted under various conditions, such as different temperatures. The main dataset consisted of a total of 350 samples. Of these, 70 % were allocated for training and the remaining 30 % for testing.

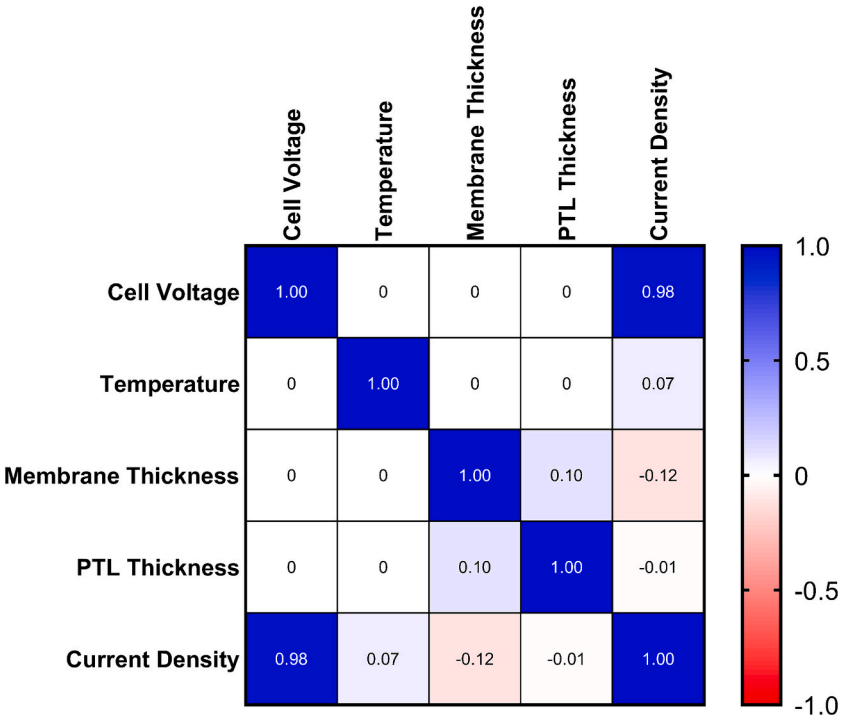

Fig. 11. Pearson correlation matrix of the variables in the dataset.

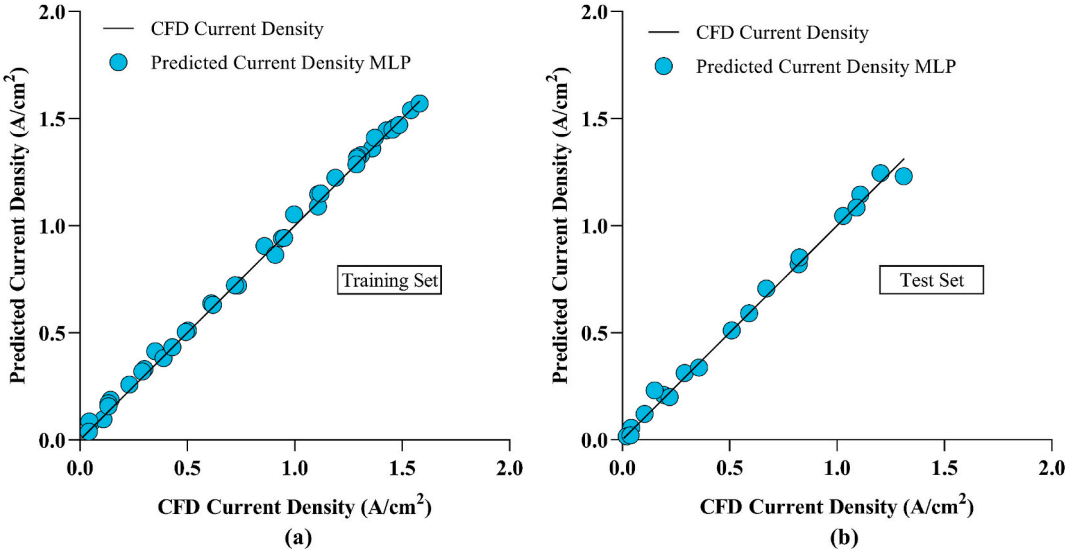

Fig. 12. MLP prediction results.

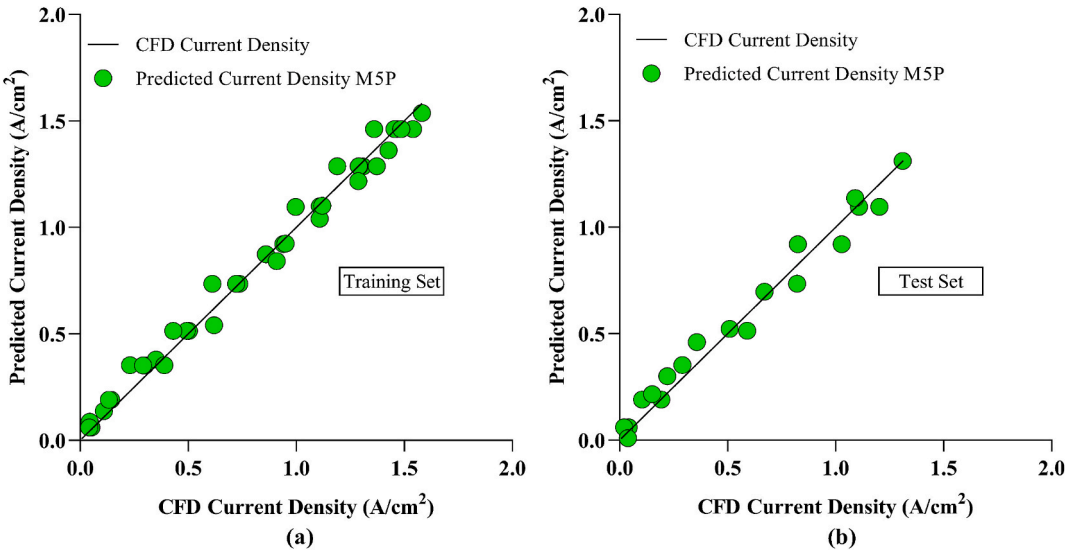

Fig. 13. M5P prediction outcomes.

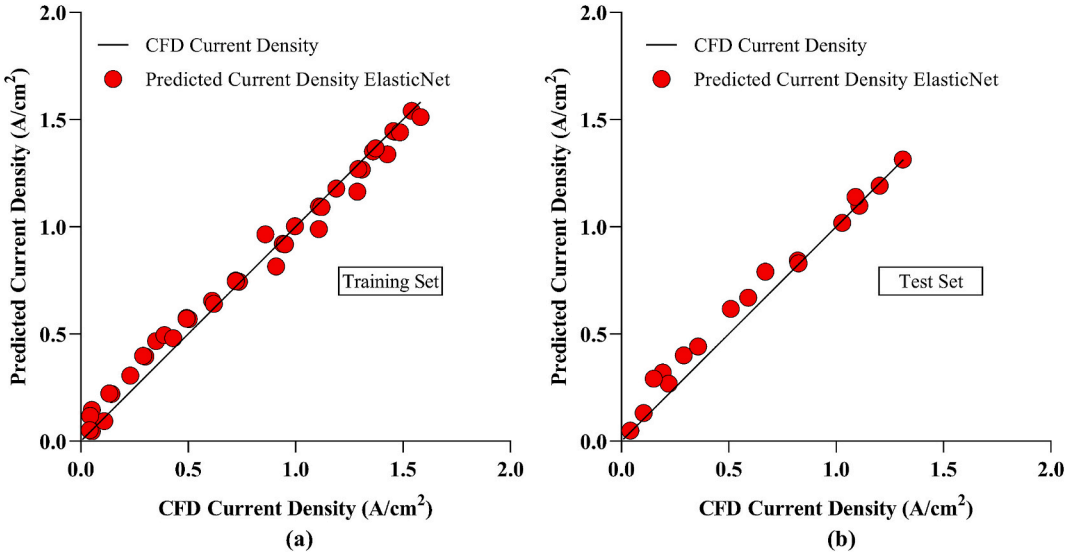

Fig. 14. ElasticNet prediction outputs.

Care was taken to ensure that the training and test sets contained distinct data with no overlap. Accordingly, 245 samples were used for model training, while 105 samples were used to test the models developed during the training phase. The current density prediction results were evaluated using the MAE, RMSE, R^2, and a20-index metrics. MAE and RMSE are defined by Equations 9 and 10. In these equations, y denotes the predicted value, x represents the actual value (i.e., the CFD-obtained value), and n indicates the number of samples in the dataset. In addition, the a20-index, which indicates the percentage of predicted values that fall within ±20 % of the actual values, was also computed to evaluate the practical prediction accuracy.

$$\mathrm{MAE} = \frac{|y_1 - x_1| + \cdots + |y_n - x_n}{n} \tag{9}$$

$$\mathrm{RMSE} = \sqrt{\frac{1}{n}\sum_{i=1}^{n}(y_i - x_i)^2} \tag{10}$$

Table 11 includes the statistical summary of the variables in the dataset. The table includes the mean, standard deviation, minimum, and maximum values of each variable. It can be observed that while cell voltage and temperature exhibit relatively low variation, membrane thickness, PTL thickness, and especially current density show higher standard deviation due to the wider range of values considered in the modeling. This variation is inherent to the nature of the parametric study and contributes to building a more generalized prediction model.

In order to investigate the linear relationships among the input and output variables, a Pearson correlation matrix was constructed and presented in Fig. 11. The Pearson correlation coefficient (r) ranges from −1 to + 1, where values close to + 1 indicate a strong positive linear relationship, values close to −1 indicate a strong negative linear relationship, and values near 0 suggest no linear correlation. Upon examining the results, the value of 0.98 in the matrix particularly indicates that cell voltage is the most influential and highly correlated variable affecting the current density.

In Figs. 12, 13, 14, and 15, the black y = x line represents the current density results obtained from CFD analysis. The blue, green, red, and pink circles correspond to the prediction results obtained using the MLP, M5P, ElasticNet, and SVM methods, respectively. In these plots, the proximity of the circles to the y = x line indicates good prediction

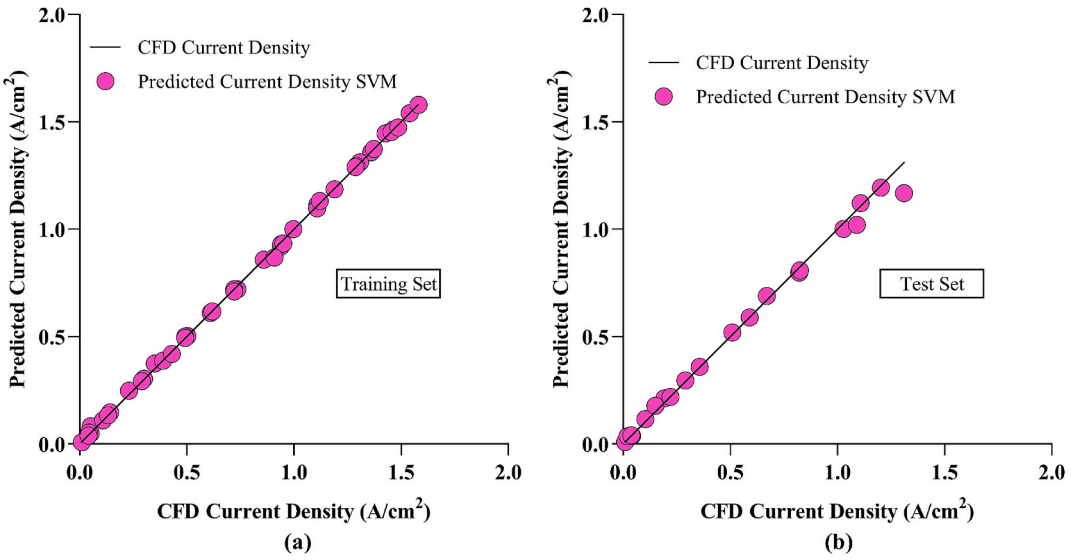

Fig. 15. SVM prediction results.

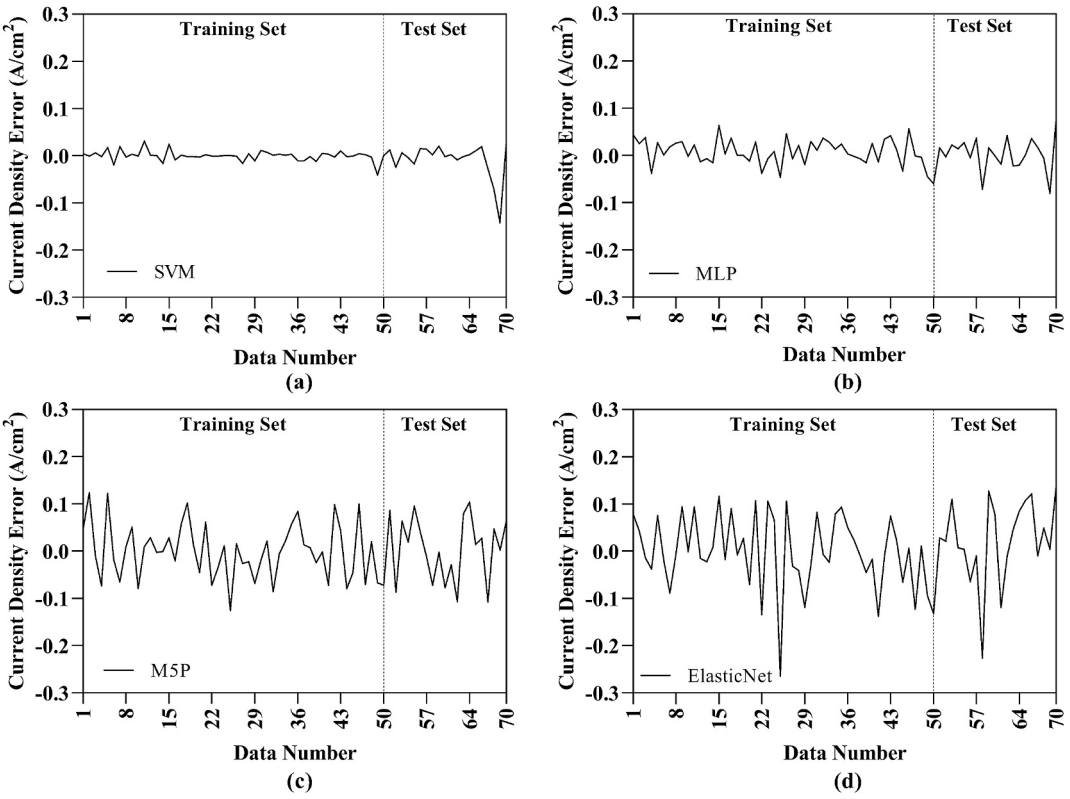

Fig. 16. Prediction errors of all methods.

performance of the machine learning method, while greater deviations from the line suggest poorer predictive accuracy.

Fig. 12 presents the prediction results obtained using the MLP method for both the training and test datasets. The results shown in Fig. 12a indicate that the MLP model achieved an MAE of 0.0220 and an RMSE of 0.0272 on the training set. The findings in Fig. 12b reveal that the model reached an MAE of 0.0283 and an RMSE of 0.0374 on the test set.

Fig. 13 presents the current density prediction results obtained using the M5P method for both the training and test datasets. As shown in Fig. 13a, the M5P algorithm predicted current density on the training set with an MAE of 0.0464 and an RMSE of 0.0581. On the other hand, the test set results presented in Fig. 13b indicate that current density was predicted by the M5P algorithm with an MAE of 0.0574 and an RMSE of 0.0670.

Fig. 14 presents the current density prediction outputs obtained using the ElasticNet method for both the training and test datasets. The results shown in Fig. 14a indicate that the ElasticNet model predicted current density on the training set with an MAE of 0.0591 and an RMSE of 0.0774. Additionally, analysis of the test set predictions presented in Fig. 14b shows that current density was estimated by ElasticNet with an MAE of 0.0715 and an RMSE of 0.0927.

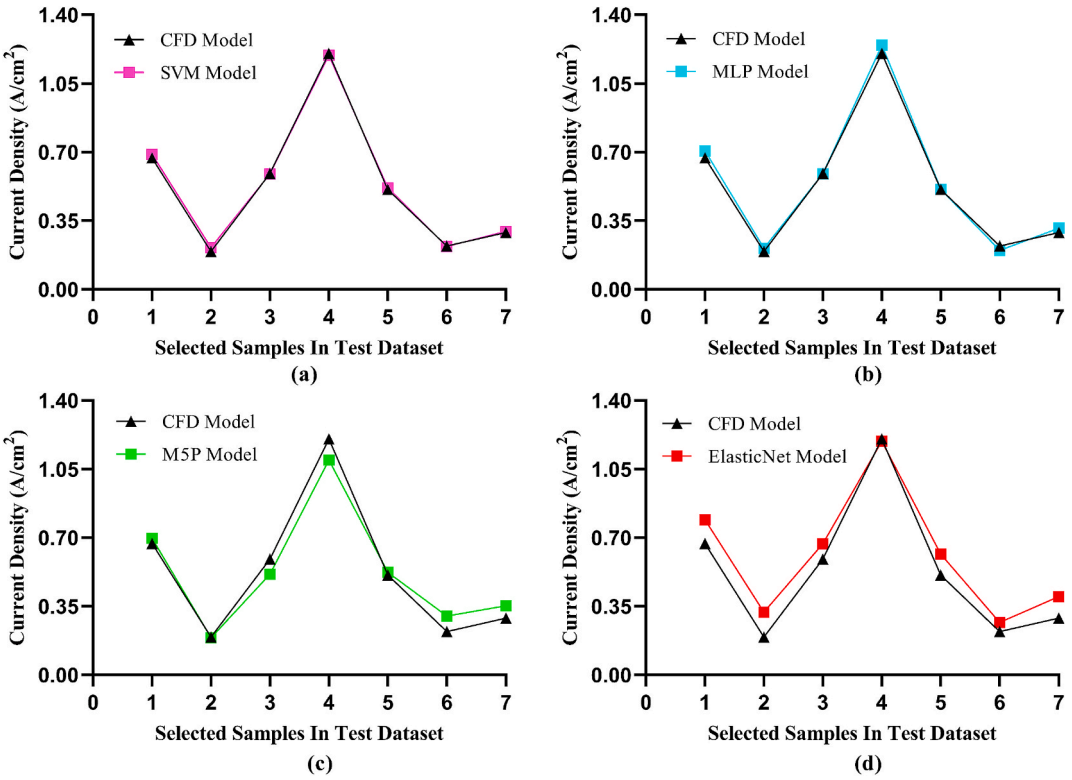

Fig. 17. Comparison of CFD current density with ML predictions for selected test samples.

Fig. 15 illustrates the prediction performance of the SVM method in estimating current density for both the training and test datasets. As seen in Fig. 15a, the SVM model demonstrates strong performance on the training set, as evidenced by the near-perfect alignment of the pink circles with the y = x line. Accordingly, current density was predicted by the SVM algorithm with an MAE of 0.0068 and an RMSE of 0.0108 on the training set. The results shown in Fig. 15b indicate that SVM predicted current density on the test set with an MAE of 0.0202 and an RMSE of 0.0371. Compared to the other three methods, the lower degree of deviation from the diagonal line in the test set suggests that the SVM method provided superior predictive performance.

Fig. 16 presents the prediction errors obtained from the SVM, MLP, M5P, and ElasticNet methods, covering both the training and test datasets. In this figure, the "error" values shown on the y-axis represent the difference between the predicted current density and the CFD-derived current density. The x-axis denotes the corresponding data number from the training and test sets. Fig. 16a, 16b, 16c, and 16d illustrate the prediction errors for the SVM, MLP, M5P, and ElasticNet methods, respectively, using black lines. In these plots, the zero point on the y-axis indicates a perfect match between the machine learning prediction and the CFD value—that is, an error-free prediction. Larger deviations from zero suggest lower prediction accuracy, while smaller deviations indicate better performance.

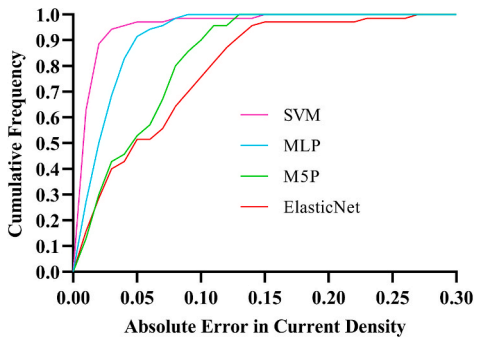

Fig. 18. Cumulative frequency results of all prediction methods.

An examination of the prediction errors presented in Fig. 16a reveals that the errors obtained using the SVM method in the training set remain very close to the y = 0 line. Although the prediction errors increase slightly in the test set compared to the training set, they remain relatively low for most data points, especially when compared to the other three methods. The maximum prediction errors observed with the SVM method were 0.041 A/cm^2 in the training set and 0.142 A/cm^2 in the test set. Analysis of the prediction errors shown in Fig. 16b indicates that the MLP method performs slightly behind the SVM approach. The maximum current density prediction errors using MLP were 0.063 A/cm^2 and 0.08 A/cm^2 for the training and test sets, respectively. In Fig. 16c, the prediction errors of the M5P method exhibit higher fluctuations, suggesting weaker performance compared to SVM and MLP. The maximum current density errors caused by M5P were 0.125 A/cm^2 in the training set and 0.108 A/cm^2 in the test set. Lastly, the error values shown in Fig. 16d indicate that ElasticNet produced larger deviations from the y = 0 line compared to SVM, MLP, and M5P, placing it behind the other three methods in terms of prediction performance. The maximum prediction errors observed using ElasticNet were 0.264 A/cm^2 for the training set and 0.226 A/cm^2 for the test set.

Fig. 17 illustrates the degree of agreement between the machine learning models and the CFD model for selected test set samples. In this figure, the current density values obtained from the CFD model are represented by black triangles, while the predictions from the SVM, MLP, M5P, and ElasticNet models are illustrated using pink, blue, green, and red squares, respectively. The results in Fig. 17a show that for all selected samples, the black triangles and pink squares overlap, indicating that the SVM model demonstrates a high level of agreement with the CFD model. In Fig. 17b, it can be observed that the MLP model also shows a high degree of consistency with the CFD results, although it slightly lags behind the SVM model, as minor deviations between the black triangles and blue squares are evident in a few instances. Analysis

Table 12
Performance comparison of all ML methods.

Estimated Parameter	*Performance Metric*	*Dataset*	*Machine Learning Method*			
			SVM	MLP	M5P	Elastic Net
Current Density	R^2	Training	0.9996	0.9976	0.9878	0.9785
		Test	0.9953	0.9931	0.9769	0.9629
	MAE	Training	0.0068	0.0220	0.0464	0.0591
		Test	0.0202	0.0283	0.0574	0.0715
	RMSE	Training	0.0108	0.0272	0.0581	0.0774
		Test	0.0371	0.0374	0.0670	0.0927
	a20-index (%)	Training	93.9	79.6	71.4	67.4
		Test	90.5	71.4	61.9	58.6

of Fig. 17c reveals that the M5P model performs noticeably worse than the SVM and MLP models, as discrepancies between the black triangles and green squares are more pronounced. Finally, Fig. 17d shows that the ElasticNet model exhibits the weakest agreement with the CFD model among the four methods, with significant mismatches between the black triangles and red squares observed for the majority of the selected data points.

Fig. 18 presents the cumulative frequency analysis results of the prediction errors obtained from all applied methods. Conducting a cumulative frequency analysis of the errors is crucial for assessing which machine learning algorithm demonstrates superior prediction performance. In this figure, the cumulative frequency curves for the SVM, MLP, M5P, and ElasticNet methods are represented by pink, blue, green, and red lines, respectively. A curve closer to the vertical y-axis indicates that a larger proportion of the data points are predicted with lower error. Upon examination of the results, it is observed that 96 % of the data were predicted with an absolute error below 0.04 by the SVM method. This rate is 83 % for MLP, 46 % for M5P, and 43 % for ElasticNet.

Table 12 shows the comparison of error values acquired with all ML methods. When the results presented in Table 12 are examined, it is observed that the SVM method outperforms the other three methods in all performance metrics.

5. Conclusions

The production of green hydrogen utilizing PEM water electrolysis technology represents a highly promising pathway with considerable potential for commercialization. The physical complexity of Proton Exchange Membrane Electrolyzer (PEMWE) systems makes accurate modeling and simulation challenging. Existing numerical models in the literature are limited in their ability to effectively represent the intricate processes of PEMWE, which include multiphase flow, electrochemical reactions, and the transfer of mass and heat. Machine learning algorithms provide notable benefits for creating computational fluid dynamics (CFD) models for electrolyzer systems, including savings in both time and energy. These systems often require substantial computational resources and time due to their complexity. Consequently, machine learning emerges as an appealing approach to enhance prediction performance. In this investigation, four machine learning models were used to compare their accuracy in predicting current density, including Support Vector Machine (SVM), Multilayer Perceptron (MLP), M5P, and Elastic Net. PEMEL design conditions, such as PTL thickness and membrane thickness, along with operating conditions like cell voltage and temperature, serve as input feature variables. The predicted current density is the output parameter. The SVM demonstrated the highest predictive accuracy among the models evaluated, achieving an MAE of 0.0068 and an RMSE of 0.0108 based on a training set, while an MAE of 0.0202 and an RMSE of 0.0371 based on a testing set. The numerical results indicate that the SVM algorithm achieves high accuracy, with 96 % of the predicted values remaining below the 0.04 threshold for absolute error.

The primary limitation of the current study lies in its reliance on CFD-generated data under controlled boundary conditions, which may not fully reflect the uncertainties and variabilities present in real-world PEM water electrolyzer operations. Additionally, while the dataset was sufficient for comparative analysis, the generalizability of the trained models could be improved through larger, experimentally validated datasets. Another limitation is that hyperparameter optimization was conducted manually, which, although effective for the dataset size, may not explore the full parameter space as thoroughly as automated optimization techniques. To overcome these limitations, future work should focus on integrating experimental PEMWE data with the CFD results to enhance model robustness and real-world applicability. Furthermore, employing advanced hyperparameter tuning methods such as Bayesian optimization or GridSearchCV would allow for a more exhaustive search and potentially improve model performance.

By evaluating four distinct machine learning approaches, the study provides a holistic assessment of their suitability for current density prediction in terms of accuracy, robustness, and interpretability. This enables researchers to better understand the trade-offs and practical applicability of each model in the context of PEMWE performance estimation. One of the key implications of this work is that these ML models can potentially be integrated into real-time control systems of experimental PEMWE setups in the future. Such integration may help reduce experimental costs by minimizing trial-and-error testing and enabling adaptive system control based on predictive insights. In addition, if appropriately trained with data from degraded or faulty operating states, ML algorithms could indeed be capable of recognizing signatures of performance decline or malfunction. By analyzing patterns and deviations in predicted vs. actual behavior, the models may assist in identifying the onset and possibly the source of system faults. Thus, the findings of this study form a foundation for future studies aimed at real-time monitoring and predictive maintenance of PEMWE systems using machine learning techniques.

CRediT authorship contribution statement

Safiye Nur Ozdemir: Writing – review & editing, Writing – original draft, Supervision, Software, Methodology, Investigation, Data curation, Conceptualization. **Oguzhan Pektezel:** Writing – review & editing, Writing – original draft, Software, Resources, Methodology, Investigation, Conceptualization.

Declaration of competing interest

The authors declare that they have no known competing financial interests or personal relationships that could have appeared to influence the work reported in this paper.

Data availability

The authors do not have permission to share data.

References

[1] Shiva Kumar S, Himabindu V. (2019). Hydrogen production by PEM water electrolysis – A review. Materials Science for Energy Technologies 2019;2(3): 442–454. KeAi Communications Co.

[2] Maghfuri AM, Kuku M. Optimized hydrogen production through machine learning: comparative analysis of electrolyzer technologies using hybrid renewable energy. Appl Therm Eng 2025;276:126923.

[3] Grigoriev SA, Porembsky VI, Fateev VN. Pure hydrogen production by PEM electrolysis for hydrogen energy. Int J Hydrogen Energy 2006;31(2):171–5. https://doi.org/10.1016/j.ijhydene.2005.04.038.

[4] Astriani Y, Tushar W, Nadarajah M. Optimal planning of renewable energy park for green hydrogen production using detailed cost and efficiency curves of PEM electrolyzer. Int J Hydrogen Energy 2024;79:1331–46. https://doi.org/10.1016/j.ijhydene.2024.07.107.

[5] Sharshir SW, Joseph A, Elsayad MM, Tareemi AA, Kandeal AW, Elkadeem MR. A review of recent advances in alkaline electrolyzer for green hydrogen production: Performance improvement and applications. Int J Hydrogen Energy 2024;49: 458–88.

[6] Akyüz ES, Telli E, Farsak M. Hydrogen generation electrolyzers: Paving the way for sustainable energy. Int J Hydrogen Energy 2024;81:1338–62.

[7] Clapp M, Zalitis CM, Ryan M. Perspectives on current and future iridium demand and iridium oxide catalysts for PEM water electrolysis. Catal Today 2023;420: 114140.

[8] Verma J, Goel S. Cost-effective electrocatalysts for hydrogen evolution reactions (HER): challenges and prospects. Int J Hydrogen Energy 2022;47(92):38964–82.

[9] Mirshekari G, Ouimet R, Zeng Z, Yu H, Bliznakov S, Bonville L, et al. High-performance and cost-effective membrane electrode assemblies for advanced proton exchange membrane water electrolyzers: long-term durability assessment. Int J Hydrogen Energy 2021;46(2):1526–39.

[10] Hu C, Wang J, Xu Y, Fu X, Deng Z, Kim JS, et al. A CFD model for analyzing multiphysics coupling and efficiency optimization in a PEMEC. J Power Sources 2025;625:235678.

[11] Wang ZR, Ao Y, Yu Y, Zhang T, Li G, Xie L, et al. Comparative study on the performance of proton exchange membrane electrolyzer with nickel foam as flow channel ribs. Int J Hydrogen Energy 2025;117:337–52.

[12] Tirumalasetti PR, Weng FB, Dlamini MM, Jung G. bin, Yu JW, Hung CC, Nelli D, Hung BS, Chiu PC. A comparative numerical analysis of proton exchange membrane water electrolyzer using different flow field dynamics. International Journal of Hydrogen Energy 2024;65:572–581.

[13] Saidi S, Brahim T, Rejeb O, Jemni A. Electrochemical and thermodynamic modeling of PEM electrolyzer performance: a comparative study with and without diffusion overpotential. Int J Hydrogen Energy 2025;128:697–712.

[14] Dang DK, Zhou B. Numerical analysis of bubble behavior in proton exchange membrane water electrolyzer flow field with serpentine channel. Int J Hydrogen Energy 2024;88:688–701.

[15] Zhu Y, Zhang Y, Bin S, Chen Z, Zhang F, Gong S, et al. Effects of key design and operating parameters on the performance of the PEM water electrolysis for hydrogen production. Renew Energy 2024;235:121290.

[16] Afshari E, Khodabakhsh S, Jahantigh N, Toghyani S. Performance assessment of gas crossover phenomenon and water transport mechanism in high pressure PEM electrolyzer. Int J Hydrogen Energy 2021;46(19):11029–40.

[17] Liao L, Li M, Yin Y, Tan X, Du R, Zhong Q, et al. Ti-mesh bipolar plate design and optimization for enhanced PEM electrolyzer performance in water splitting. Int J Hydrogen Energy 2024;64:981–9.

[18] Lin R, Lu Y, Xu J, Huo J, Cai X. Investigation on performance of proton exchange membrane electrolyzer with different flow field structures. Appl Energy 2022;326: 120011.

[19] Toghyani S, Afshari E, Baniasadi E, Atyabi SA, Naterer GF. Thermal and electrochemical performance assessment of a high temperature PEM electrolyzer. Energy 2018;152:237–46.

[20] Yan Y, Li P, Zhao S, Luo K, Huang S, Duan Z, et al. Study on a 3D multi-physics coupled model for a PEM electrolyzer with an imitation water droplet ribbed column flow field. Int J Hydrogen Energy 2025;103:428–45.

[21] Ozdemir S, Taymaz I, Okumuş E, Gül Boyacı San F, Akgün F. Experimental investigation on performance evaluation of PEM electrolysis cell by using a Taguchi method. Fuel 2023;344:128021.

[22] Xu B, Yang Y, Li J, Ye D, Wang Y, Zhang L, et al. A comprehensive study of parameters distribution in a short PEM water electrolyzer stack utilizing a full-scale multi-physics model. Energy 2024;300:131565.

[23] Li H, Inada A, Fujigaya T, Nakajima H, Sasaki K, Ito K. Effects of operating conditions on performance of high-temperature polymer electrolyte water electrolyzer. J Power Sources 2016;318:192–9.

[24] Noor Azam AMI, Li NK, Zulkefli NN, Masdar MS, Majlan EH, Baharuddin NA, et al. Parametric study and electrocatalyst of polymer electrolyte membrane (PEM) electrolysis performance. Polymers 2023;15(3):560.

[25] Madhavan PV, Moradizadeh L, Shahgaldi S, Li X. Data-driven modelling of corrosion behaviour in coated porous transport layers for PEM water electrolyzers. Artificial Intelligence Chemistry 2025;3:100086.

[26] Ozdemir SN, Pektezel O. Performance prediction of experimental PEM electrolyzer using machine learning algorithms. Fuel 2024;378:132853.

[27] Hayatzadeh A, Fattahi M, Rezaveisi A. Machine learning algorithms for operating parameters predictions in proton exchange membrane water electrolyzers: Anode side catalyst. Int J Hydrogen Energy 2024;56:302–14.

[28] Shomope I, Al-Othman A, Tawalbeh M, Alshraideh H, Almomani F. Machine learning in PEM water electrolysis: a study of hydrogen production and operating parameters. Comput Chem Eng 2025;194:108954.

[29] Tawalbeh M, Shomope I, Al-Othman A, Alshraideh H. Prediction of hydrogen production in proton exchange membrane water electrolysis via neural networks. Int J Thermofluids 2024;24:100849.

[30] Ham K, Bae S, Lee J. Classification and technical target of water electrolysis for hydrogen production. J Energy Chem 2024;95:554–76.

[31] Toghyani S, Afshari E, Baniasadi E. Three-dimensional computational fluid dynamics modeling of proton exchange membrane electrolyzer with new flow field pattern. J Therm Anal Calorim 2019;135(3):1911–9.

[32] Ansys. Ansys fluent theory guide. ANSYS Inc.; 2024.

[33] Mutu HB. Machine learning-based approach for ballistic performance prediction of hybrid armors. Mater Today Commun 2025;47:113226.

[34] Akay OE, Das M. Modeling the total heat transfer coefficient of a nuclear research reactor cooling system by different methods. Case Stud Therm Eng 2021;25: 100914.

[35] Alzubi J, Nayyar A, Kumar A. Machine learning from theory to algorithms: an overview. J Phys Conf Ser 2018;1142:012012.

[36] Rajasundrapandiyanleebanon T, Kumaresan K, Murugan S, Subathra M, Sivakumar M. Solar energy forecasting using machine learning and deep learning techniques. Arch Comput Meth Eng 2023;30:3059–79.

[37] Allal Z, Noura HN, Salman O, Chahine K. Machine learning solutions for renewable energy systems: applications, challenges, limitations, and future directions. J Environ Manage 2024;354:120392.

[38] Lee H, Kim D, Gu J-H. Prediction of food factory energy consumption using MLP and SVR algorithms. Energies 2023;16:1550.

[39] Siqueira Nascimento ASB de, Machado JPZ, Santos Coelho L. dos, Flesch RCC. Evaporating temperature estimation of refrigeration systems based on vibration data-driven soft sensors. International Journal of Refrigeration 2024;168:288-296.

[40] Laidi M, Hanini S. Optimal solar COP prediction of a solar-assisted adsorption refrigeration system working with activated carbon/methanol as working pairs using direct and inverse artificial neural network. Int J Refrig 2013;36:247–57.

[41] Behnood A, Behnood V, Gharehveran MM, Alyamac KE. Prediction of the compressive strength of normal and high-performance concretes using M5P model tree algorithm. Constr Build Mater 2017;142:199–207.

[42] Nhu V-H, Shahabi H, Nohani E, Shirzadi A, Al-Ansari N, Bahrami S, et al. Daily water level prediction of Zrebar Lake (Iran): a comparison between M5P, random forest, random tree and reduced error pruning trees algorithms. Int J Geo-Inform 2020;9:479.

[43] Behnood A, Daneshvar D. A machine learning study of the dynamic modulus of asphalt concretes: an application of M5P model tree algorithm. Constr Build Mater 2020;262:120544.

[44] Hans C. Elastic net regression modeling with the orthant normal prior. J Am Stat Assoc 2011;106:1383–93.

[45] Pektezel O, Das M, Ibrahim AH. Experimental analysis of different refrigerants' thermal behavior and predicting their performance parameters. J Thermophys Heat Transfer 2023;37:309–19.

[46] Pektezel O, Das M, Acar HI. Experimental exergy analysis of low-GWP R290 refrigerant and derivation of exergetic performance equations with regression algorithms. Int J Exergy 2023;40:467–82.

[47] Li M, Niu D, Ji Z, Cui X, Sun L. Forecast research on multidimensional influencing factors of global offshore wind power investment based on random forest and elastic net. Sustainability 2021;13:12262.

[48] Giglio C, Brown SD. Using elastic net regression to perform spectrally relevant variable selection. J Chemom 2018;32:e3034.

[49] Mohanasundaram V, Rangaswamy B. Elastic net with bayesian density estimation model for feature selection for photovoltaic energy prediction. Sci Rep 2025;15: 8736.

[50] Zayed ME, Kabeel A, Shboul B, Ashraf WM, Ghazy M, Irshad K, et al. Performance augmentation and machine learning-based modeling of wavy corrugated solar air collector embedded with thermal energy storage: support vector machine combined with Monte Carlo simulation. J Storage Mater 2023;74:109533.

[51] Chen J-L, Liu H-B, Wu W, Xie D-T. Estimation of monthly solar radiation from measured temperatures using support vector machines–a case study. Renew Energy 2011;36:413–20.

[52] Üstün B, Melssen WJ, Buydens LMC. Facilitating the application of support vector regression by using a universal pearson VII function based kernel. Chemom Intel Lab Syst 2006;81:29–40.

[53] The University of Waikato, WEKA: Waikato Environment for Knowledge Analysis, Version 3.8.5, Hamilton, New Zealand, 2020.

[54] Debe MK, Hendricks SM, Vernstrom GD, Meyers M, Brostrom M, Stephens M, et al. Initial performance and durability of ultra-low loaded NSTF electrodes for PEM electrolyzers. J Electrochem Soc 2012;159. K165–76.